A CFD Investigation into Ground Effect Aerodynamics

by

Emanuela Genua

Submitted to the Department of Aerospace Design, Integration and Operations
in partial fulfillment of the requirements for the degree of

Master of Science in Aerospace Engineering

at

Delft University of Technology

July 2009

Thesis Supervisor
Marc I. Gerritsma
Associate Professor

Preface

This thesis report is the result of the work performed as final graduation project for the Master Program in Aerospace Engineering at Delft University of Technology. The research here presented has been carried out in close cooperation with Actiflow B.V.

The main subject of this thesis is a numerical investigation into ground effect aerodynamics with a focus on those aspects more relevant to the automotive industry. The investigation can be divided into two main parts. In the first stage a study on the aerodynamics of a 2D inverted airfoil in ground effect has been performed. The main outcome of this part of the research is the identification of an optimal range of mesh characteristics within which the main features of the flow are correctly captured numerically solving RANS equations. The conclusions drawn for the airfoil serve as starting point for the second stage of the study: an investigation into the aerodynamics of a bluff body equipped with a diffuser in ground effect.

The present report consists of two papers. Each paper deals with one part of the research. Readers of this document should preferably have some prior knowledge about aerodynamics and computational fluid dynamics.

I wish to thank Eric Terry and Roy Campe for this opportunity and all the Actiflow staff for the technical support and their pleasant company. I'm very grateful to Prof. Gerritsma for the academic supervision he continuously provided me, for his critical insights and for his patience. Many thanks go to my parents who have supported me financially and morally during all these years of studying; none of this would have been possible without their help.

Emanuela Genua
Delft, July 9, 2009

A CFD Investigation of an Inverted Airfoil in Ground Effect

Emanuela Genua

Delft University of Technology, Delft 2629HS, The Netherlands

Actiflow BV, Breda 4823AD, The Netherlands

A computational study of the flow around an inverted 2D airfoil in ground effect is performed. The effect of mesh parameters and turbulence model on the solution is thoroughly investigated. Results are compared to previous works found in literature and an improvement in CFD predictive capabilities is noticeable. *Spalart-Allmaras* shows to be the most accurate and robust turbulence model among the ones tested. An optimal range of mesh characteristics is identified. Within this range the main features of the flow, including separation due to adverse pressure gradient and subsequent downforce reduction, are correctly captured.

Nomenclature

α	angle of attack
AR	aspect ratio
c	airfoil chord
C_d	drag coefficient
C_l	downforce coefficient
C_p	pressure coefficient
h	ride height
ν	kinematic air viscosity
p	static pressure
q_∞	free stream dynamic pressure
ρ	air density
Re	Reynolds number
u, v	velocity components
u_∞	free stream velocity
y^+	normalized distance from the wall

I. Introduction

An inverted airfoil in ground effect may be considered a simplified representation of the front wing of a race car. The aerodynamics of the front wing is crucial since it contributes for about 30%[17] to the total downforce of the car and because the air that flows over and under the front wing enters the undertray, influencing the underbody flow. Of fundamental importance is, in particular, the understanding of the relation between downforce generated and distance of the wing from the ground.

For an inverted airfoil the effect of decreasing the ride height is similar to increasing the angle of attack of a regular airfoil: as for a regular airfoil, the lift increases with the angle of attack until a maximum is reached and the wing stalls; the downforce generated by an inverted airfoil in ground effect, increases as the ride height is reduced up to a critical point after which the downforce drops. Extensive literature can be found on the subject.[5,9–12,15,17,18]

Ranzenbach and Barlow[10–12] investigated the effect of ride height reduction using wind tunnel testing. The ground was a fixed wall. The downforce was seen to increase as the ride height was reduced until a maximum was reached. As the ride height was further reduced, downforce reduction was observed. Ranzenbach and Barlow claimed that the downforce reduction phenomenon was due to the fact that, after a critical ride height, the ground and airfoil boundary layers merged, limiting the amount of air that could flow between the airfoil and the ground.

A more recent and detailed study on the aerodynamics of a highly cambered single element wing in ground effect was carried out by Zerihan and Zhang.[5,15,17,18] The study was performed in a wind tunnel equipped with a moving belt.

Zerihan and Zhang found the same qualitative downforce behavior as Ranzenbach and Barlow, but they gave a different explanation for the downforce reduction phenomenon: since the critical ride height at which downforce reduction occurred was observed to be independent of the Reynolds number, they inferred that the physical mechanism underneath the downforce reduction phenomenon could not be the merging of the boundary layers. In fact, the merging of the boundary layers observed by Ranzenbach and Barlow was most likely due to the use of a fixed ground, which cannot appropriately simulate road conditions.

Zerihan and Zhang report that the downforce reduction phenomenon is instead caused by a large region of separated flow at the trailing edge. As the airfoil is moved closer and closer to the ground, the air speed underneath the airfoil increases with a simultaneous strengthening of the adverse pressure gradient at the trailing edge, leading to separation. As the ride height is further reduced, the separation point moves forward, until the separated region is too big and the downforce drops.

Computational studies have been performed too. Ranzenbach and Barlow[10,12] performed RANS simulations using a $k-\epsilon$ turbulence model. In Ref. 17 Zerihan and Zhang solved the unsteady RANS equations modeling the turbulence with *Spalart-Allmaras* and $k-\omega$ *SST*, while in Ref. 5 Mahon and Zhang performed steady calculations using *Realizable* $k-\epsilon$. Overall they all found good qualitative results compared with their respective experiments.

In this paper, a numerical investigation into the aerodynamics of a 2D inverted airfoil in ground effect is reported. The goal of the research is to clarify the effect of grid refinement, mesh parameters, turbulence models and boundary layer modeling, on the predicted downforce behavior for different ride heights.

II. Computational Modeling

A. Airfoil Geometry

The study is performed on the airfoil Tyrrell026, the main element of the front wing of the Tyrrell Formula One car that competed in the 1998 season. This airfoil stems from modifications to the NASA-LANGLEY LS(1)-0413MOD profile. The complete listing of the profile at $\alpha = 3.6°$ can be found in Ref. 16 . Note that for an inverted airfoil the angle of attack is defined positive for a rotation that brings the leading edge closer to the ground.

The original airfoil has a chord length of 223.4 mm and a finite trailing edge thickness of $0.007c$. In order to avoid meshing problems the trailing edge has been sharpened using the program XFOIL. For the complete listing of the modified airfoil Tyrrell026S, see Table 1.

The distance between the lower point on the suction surface and the ground will be referred to as ride height h.

In Figure 1 the geometry and the coordinate system is depicted.

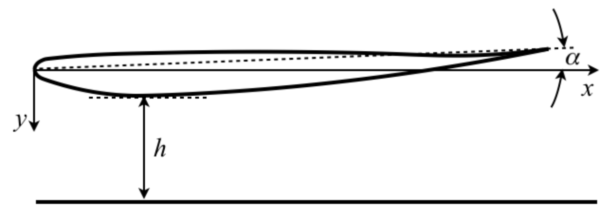

Figure 1. Airfoil geometry and coordinate system.

B. Flow Conditions

All the simulations are performed at a Reynolds number based on the chord length of $4.6 \cdot 10^5$ corresponding to a free stream velocity of 30 m/s.

The free stream turbulence level has been set to 0.3%. These conditions correspond to experimental conditions as in Ref. 5, 15, 17.

The integral length scale of the turbulence is set to 1 cm, typical for wind tunnel experiments.[1]

No transition from laminar to turbulent flow is simulated; the flow is assumed to be fully turbulent.

C. Governing Equations

The steady Reynolds-averaged Navier-Stokes equations are solved using OpenFOAM.

$$\frac{\partial \overline{u}_i}{\partial x_i} = 0 \tag{1}$$

$$\overline{u}_j \frac{\partial \overline{u}_i}{\partial x_j} = -\frac{1}{\rho}\frac{\partial \overline{p}}{\partial x_i} + \nu \frac{\partial^2 \overline{u}_i}{\partial x_j^2} - \frac{\partial \overline{u_i' u_j'}}{\partial x_j} \tag{2}$$

The convergence criterion is based on the aerodynamic forces on the airfoil: when downforce and drag were observed to reach steady state values, simulations were stopped. The number of iterations required varies from 2000 to 5000 when a turbulence model is used, and from 7000 to 15000 when the equations are solved up to the wall.

D. Grid Structure

The computational grids are designed using ANSA. For different ride heights the general topology of the grid is fixed.

Every mesh consists of three blocks: two structured grids are folded around the airfoil and along the ground, whereas the rest of the computational domain is unstructured. In order to avoid non-orthogonal cells at the trailing edge, and to refine the wake region, a fictitious surface was created, extending from the trailing edge to the outflow boundary, and meshed together with the airfoil. In Figure 2 and Figure 3 it is shown the augmented quality of the prism cells wrapped around the airfoil with the aid of the fictitious surface.

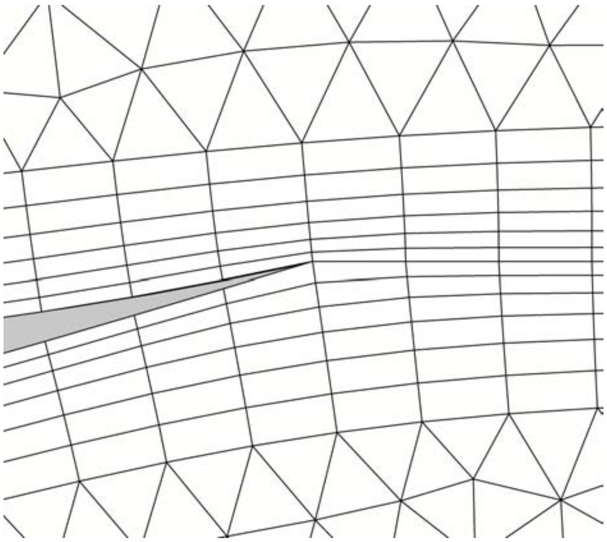

Figure 2. Prism layers folded around the airfoil using the fictitious surface extending from the trailing edge.

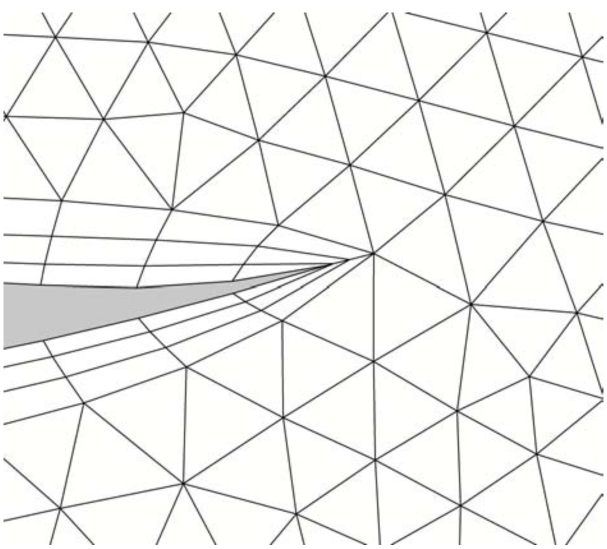

Figure 3. Prism layers folded around the airfoil without the fictitious surface extending from the trailing edge.

The upstream and downstream boundaries of the computational domain are placed respectively at $2c$ and $5c$ from the airfoil leading edge. The distance of the upper boundary of the computational domain from the ground is of $6.8c$, according to Ref. 5. Tests were performed with a significantly larger computational domain (four times as large), but no differences in solutions were observed.

Depending on the ride height and on mesh parameters, the total number of cells varies from 7900 to 141000.

E. Boundary Conditions

Airfoil and ground plane are modeled as solid walls at which a no-slip boundary condition is imposed. Furthermore, in order to correctly simulate the ground effect, on the ground plane a tangential velocity equal to the free stream speed is enforced.

At the upstream boundary a uniform velocity inlet and a zero pressure gradient condition are prescribed, whereas at the downstream boundary a zero velocity gradient and a uniform pressure outlet are imposed.

The top boundary of the computational domain is modeled as a slip wall.

III. Grid and Turbulence Model Sensitivity Study

A sensitivity study on the influence of grid refinement and turbulence model is performed. Three significant ride heights are considered:

- Free stream, in which the airfoil is far enough from the ground that it has no influence on the aerodynamic forces.
- The height $h = 0.224c$ is chosen as representative of the downforce enhancement region, where the downforce generated by the airfoil increases with reducing ride height. According to experiments[5,15,17] at this ride height a first hint of separation at the trailing edge is present.
- The height $h = 0.09c$ is chosen as representative of the downforce reduction region, where the downforce generated by the airfoil decreases with reducing ride height because of the presence of a large area of separated flow at the trailing edge.[5,15,17]

Two grid parameters are objects of the sensitivity study: the spacing of the elements on the airfoil and ground surfaces, referred to as l, and the height of the first prism layer of the structured grids, referred to as $H_{firstlayer}$, which influences the average value of y^+. Note that a constant spacing l is used on both airfoil and ground.

The prism layers are extruded in such a way that ideally the area of each cell of the last structured layer is equal to the area of the adjacent unstructured cell. The following constraint holds:

$$H_{lastlayer} \approx \frac{\sqrt{3}}{4} l. \tag{3}$$

In particular Equation (3) determines the growing factor (1.1 or 1.2) and the number of layers to be extruded.

In Figure 4 all the relevant mesh parameters are depicted. For the sake of clarity, the cell dimensions have been amplified. Notice that the cells highlighted in grey have approximately the same area.

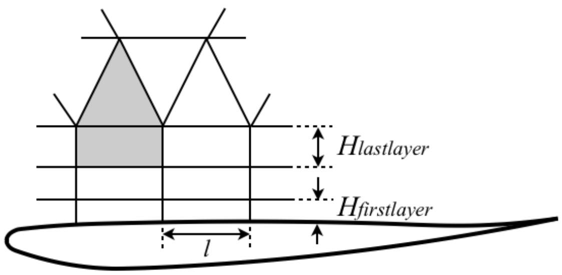

Figure 4. Mesh parameters object of the sensitivity study.

Five grids are tested with three different turbulence models implemented with wall function: *Realizable* $k-\epsilon$, $k-\omega$ *SST* and *Spalart-Allmaras*. The grids are referred to as fine, medium and coarse, depending on the length of the elements on the airfoil and ground, namely 2, 4 and 8 mm. Two different first layer heights are tested: 0.6 mm corresponding to $y^+ \approx 30$, and 1.2 mm corresponding to $y^+ \approx 60$.

Note that for the fine grid, the largest first layer height is not tested because the constraint given by (3) cannot be fulfilled.

Analogously, four grids are tested with two different turbulence models using near wall treatment: *Launder-Sharma* $k-\epsilon$ and *Spalart-Allmaras*. The grids are referred to as fine and very fine, depending on the length of the elements on the airfoil and ground, namely 2 and 1 mm. Two different first layer heights are tested: 0.01 mm corresponding to $y^+ \approx 0.5$, and 0.02 mm corresponding to $y^+ \approx 1$.

Mesh characteristics and standard notation used to uniquely identify a grid are summarized in Table 2 and Table 3. Notice that the aspect ratio as reported in the tables is defined as the length of the cell over the height.

Abbreviations are used to identify the turbulence model in the case name: RKE, KWS, SA and LSKE, indicate *Realizable* $k-\epsilon$, $k-\omega$ *SST*, *Spalart-Allmaras* and *Launder-Sharma* $k-\epsilon$ respectively.

The combinations grid-turbulence model are judged comparing the predicted downforce coefficient with experimental results, for the three ride heights considered. Notice that in this paper all the results are compared with experimental and computational results found in Ref. 17.

A. Results

1. Free Stream

Wall Function. Results are overall very good: most cases give an error below 5% with respect to experimental results.

The best performance is that of grid Med30, for all turbulence models the error is below 3%.

On the coarse grids bad convergence is observed: the solution oscillates around a good mean result. It is worth to mention that the oscillations are reduced on the coarse grids tested with *Spalart-Allmaras*.

Strangely, the fine grids do not give the best results, the error is above 5% for all turbulence models.

The best turbulence model is *Spalart-Allmaras* with a mean error below 2%, but the performances of *Realizable* $k-\epsilon$ and $k-\omega$ *SST* are very good as well, with a mean error below 3% .

Near Wall Treatment. On average the errors are higher compared to those obtained using a wall function.

Results are very good and similar to each other for all the grids tested with *Launder-Sharma* $k-\epsilon$, the error is in fact always below 3%.

On the other hand, all the grids tested with *Spalart-Allmaras* overpredict the downforce coefficient by more than 8%.

2. Downforce Enhancement Region

Wall Function. At this ride height good overall results are obtained.

No significant changes are observed in the performance of the fine grids, whereas on the coarse grids the average error increases to approximately 10% and oscillations in the converged results are again observed. As for the free stream case the coarse grids tested with *Spalart-Allmaras* perform better (error below 7%) and the oscillations in the results are reduced.

All the medium grids, with the exception of Med60RKE, correctly predict the C_l. In particular, very small errors (below 3%) are found for the Med30 grid with all turbulence models.

On average *Spalart-Allmaras* and $k-\omega$ *SST* perform well, whereas the mean error of *Realizable* $k-\epsilon$ is about 10%.

Near Wall Treatment. The performance in terms of mean error is similar to that of the wall function cases.

Again, *Launder-Sharma* $k-\epsilon$ gives very good results on all grids (errors below 2%), whereas *Spalart-Allmaras* overpredicts the downforce coefficient in the order of 10-20%.

3. Downforce Reduction Region

WALL FUNCTION. At this ride height the challenge imposed by the strong adverse pressure gradient is clearly reflected in the computational results. The best performances are obtained with Med30SA (error below 1%) and Med60SA (error below 4%). Larger errors, ranging from 10% to 30%, are found on the medium grids tested with *Realizable* $k-\epsilon$ and $k-\omega$ *SST*.

The performance of Fine30RKE and Fine30KWS are considerably less accurate: the predicted C_l values are more than 50% higher compared to experiments. Fine30SA does better, with an error below 15%.

The performance of the coarse grids does not change much compared to the downforce enhancement region.

At this ride height, all the grids tested with *Spalart-Allmaras* and *Realizable* $k-\epsilon$ predict a large area of separated flow on the trailing edge, while with none of the grids tested with $k-\omega$ *SST* separation is observed.

The best turbulence model is again *Spalart-Allmaras*, with a mean error below 1%. *Realizable* $k-\epsilon$ performs well only on Med30, whereas at this ride height $k-\omega$ *SST* does not give good results on any of the tested grids.

NEAR WALL TREATMENT. The errors are slightly higher compared to the downforce enhancement region, but again *Launder-Sharma* $k-\epsilon$ performs good and all the grids give practically the same results. Very bad predictions are obtained with *Spalart-Allmaras* (average error above 40%).

At this ride height all the grids tested with near wall treatment show separation at the trailing edge.

All the results of the grid and turbulence model sensitivity study are summarized in Table 6. Notice that in the table the rows named *Spalart-Allmaras* and $k-\omega$ *SST* refer to computational results found in literature.[17]

B. Discussion

The most striking observation is that the fine grids with wall function do not give the best results. With *Spalart-Allmaras*, C_l predictions are decent on all the three ride heights. On the other hand, *Realizable* $k-\epsilon$ and $k-\omega$ *SST* at the smallest ride height even fail to predict a downforce coefficient within a reasonable range of error.

Unsteady simulations were performed to establish whether this was due to the fact that fine grids can capture smaller oscillations length and time scales and therefore do not converge to good steady results. However the unsteady results are even less accurate, so this hypothesis is ruled out.

The most successful grid is Med30, which gives good results for all the considered ride heights with both *Realizable* $k-\epsilon$ and *Spalart-Allmaras*.

While *Spalart-Allmaras* gives good results for all ride heights on Med60, *Realizable* $k-\epsilon$ performs only well in free stream. This may be a manifestation of *Spalart-Allmaras*' robustness when used with y^+ values ranging from 30 to 60, while the prediction capabilities of *Realizable* $k-\epsilon$ decreases with increasing y^+.

The $k-\omega$ *SST* model gives very good results (errors below 3%) on Med30 and Med60, both in free stream and in the downforce enhancement region, but at the smaller ride height fails on all the grids, suggesting it can have problems dealing with strong adverse pressure gradients.

On the coarse grids the trend seems to be quite clear: the converged results contain oscillations around a good mean value, worsening with decreasing ride height.

These oscillations are most likely due to a problem at the leading edge: due to the coarseness of the mesh the stagnation point keeps shifting between two adjacent cells.

Overall, *Spalart-Allmaras* with wall function is the best and most robust turbulence model, giving good results on all the tested grids.

Very interesting is the performance of *Launder-Sharma* $k-\epsilon$ with near wall treatment: it gives good results for all three ride heights considered and the C_l values predicted on different grids are very similar, indicating a low grid sensitivity.

On the other hand, *Spalart-Allmaras* with near wall treatment presents higher error for all ride heights.

IV. Ride Height Sensitivity Study

A. First Stage

From the grid and turbulence model sensitivity study eight combinations grid-turbulence model are selected for the ride height sensitivity study. Among the near wall treatment cases, VFine1LSKE is chosen. Even though all the grids tested with *Launder-Sharma* $k-\epsilon$ give good and very similar solutions, this is the one with the smallest average error on the three ride heights. For the wall function cases, four grid-turbulence model combinations are selected because of their good performance: Med30SA, Med60SA, Med30RKE and Coa30SA. Furthermore, in order to investigate the effect of the aspect ratio of the first cell and of y^+, the ride height sensitivity study is also performed on Fine30SA, Med60RKE and Coa60SA.

The ride height ranges from $h = 0.671c$, the largest ride height in ground effect according to Ref. 15 and 17, to $h = 0.09c$. The maximum downforce has to be found at $h = 0.134c$.[17]

1. *Results*

Med30SA gives the best performance, following the experimental C_l versus ride height curve very closely. The maximum downforce is correctly predicted at $h = 0.134c$ and the mean error is below 2%. A first hint of separation at the trailing edge is observed at $h = 0.224c$ with the portion of separated flow increasing with decreasing ride height (Figure 5), in accordance with experiments.

Both Med30RKE and VFine1LSKE perform satisfactory until $h = 0.179c$. With the former the maximum in downforce is found at $h = 0.179c$, with a consequent underprediction of the C_l at smaller ride heights. This is also the ride height at which separation is firstly observed. On the other hand with VFine1LSKE, the C_l is overpredicted in $h = 0.134c$ and $h = 0.09c$. For this case, simulations are also ran at the ride height $h = 0.05c$, where the decrease in downforce is finally observed. Separated flow is observed at $h = 0.09c$ and at $h = 0.05c$.

The performance of the medium grids with higher y^+ is not as good. Med60SA underpredicts the downforce coefficient with an average error of about 5%, but the maximum is not captured at the correct ride height. On the other hand, Med60RKE fails to predict a downforce coefficient versus ride height curve within a reasonable range of error. It is the least accurate performance observed, with an average error above 15%. Both Med60SA and Med60RKE predict separation from $h = 0.179c$ onwards.

Coa30SA and Coa60SA do relatively well. With the former a first hint of separation at the trailing edge is observed at $h = 0.224c$, whereas with Coa60SA separation is postponed to $h = 0.179c$. Oscillations in the converged solutions around good mean values are still present. Even though the error is larger compared to that of Med30 grids (4% for Coa30SA and 7% for Coa60SA), the maximum is correctly predicted at $h = 0.134c$.

Fine30SA always overpredicts the C_l by about 7% and fails to predict the maximum at the correct ride height. The largest ride height at which flow separation is observed is $h = 0.179c$.

All the grids tested predicted a large area of separated flow at $h = 0.09c$, in agreement with the experiments.

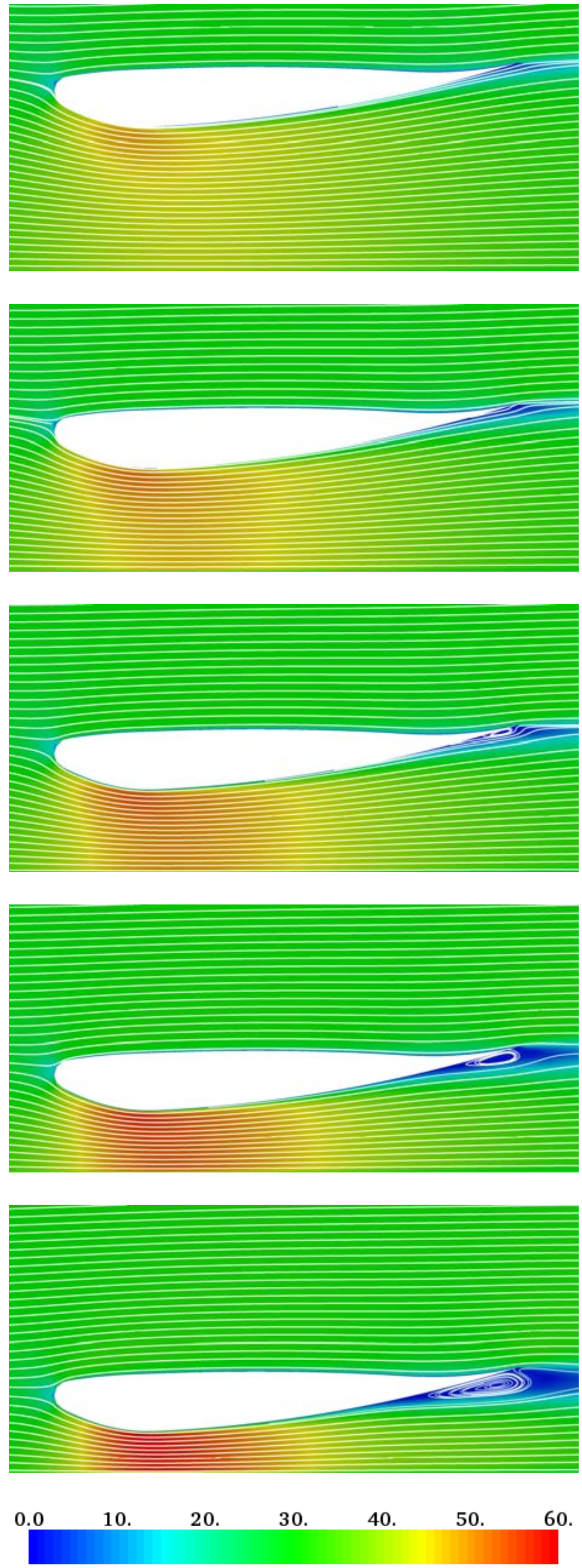

Figure 5. Velocity magnitude contour and streamlines for Med30SA at ride heigths: $h = 0.313c$, $h = 0.224c$, $h = 0.179c$, $h = 0.134c$, $h = 0.09c$.

In Figure 6 the downforce coefficient versus ride height curves for all the combinations grid-turbulence model tested are depicted. In Figure 7 the errors in the solutions for every ride height in the considered range are given in percentage of the experimental value. Notice that the curves referred to as SA and kwSST are representative of computational results found in Ref. 17.

2. *Discussion*

Overall the general behavior inferred from the grid and turbulence model sensitivity study is verified. The best obtained results are more in agreement with the experiments compared to computational results found in literature.

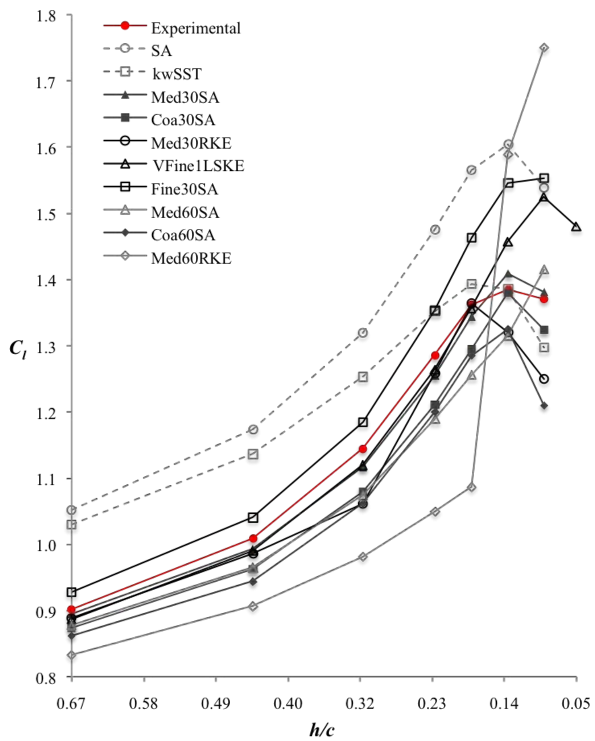

Figure 6. Downforce coefficient versus ride height for the combinations tested in the first stage of the ride height sensitivity study. The curves referred to as SA and kwSST are representative of computational results found in literature.

Spalart-Allmaras confirms to be the best and most robust turbulence model, giving good results over all ride heights for all grids.

For *Realizable* $k-\epsilon$ the hypothesis that its performance deteriorates with increasing y^+ is validated.

The only grid tested with near wall treatment, VFine1LSKE, gives decent results, even though the maximum downforce is delayed to $h = 0.09c$ and no separation is observed for larger ride heights.

From these simulations it seems that, besides the turbulence model, a major role is played by the combination of y^+ and $\mathcal{AR}$. In particular, the similarity in terms of trend and average error, between the performances of Fine30SA and Med60SA, grids with same aspect ratio of the first cell, was established. These observations are further investigated in the second stage of the ride height sensitivity study.

B. Second Stage

In this stage of the research grids are tested only with *Spalart-Allmaras* with wall function. The goal is to identify an optimal range or grid characteristics in the $y^+, \mathcal{AR}$ plane.

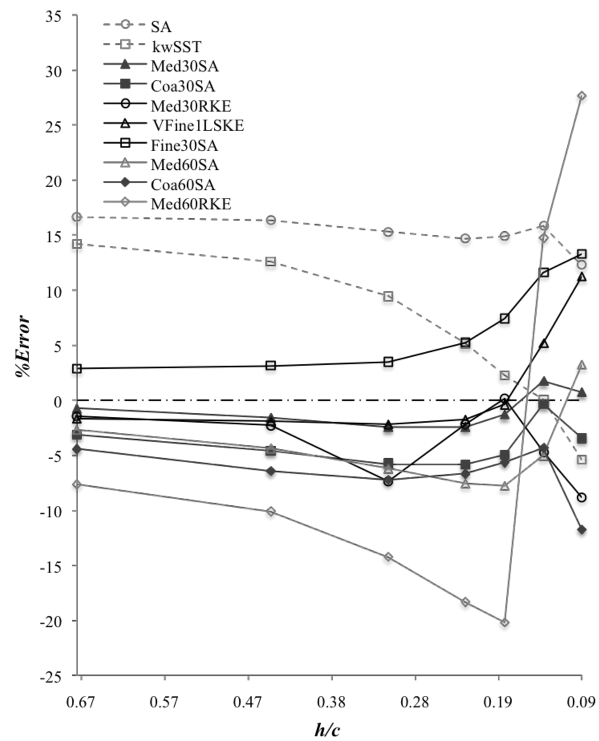

Figure 7. Errors given in percentage of the experimental downforce coefficient for the combinations tested in the first stage of the ride height sensitivity study. The curves referred to as SA and kwSST are representative of computational results found in literature

Both Fine30SA and Med60SA do not give satisfying results, so $\mathcal{AR} = 3.33$ is not tested on other grids and taken as the left boundary of the $y^+, \mathcal{AR}$ plane. The right boundary is defined at the biggest aspect ratio tested so far which is that of Coa30SA, $\mathcal{AR} = 13.33$. Since a wall function is used, the top and bottom boundary of the plane are fixed to $y^+ \approx 60$ and $y^+ \approx 30$.

From the results obtained with the grids tested at the first stage of the ride height sensitivity study, new grids are selected to explore the $y^+, \mathcal{AR}$ plane.

On the coarse grids, we find good results, but observe convergence problems due to the too big spacing of the elements on the airfoil (8mm). Three new grids are tested, with a spacing of 6mm. The first one is referred to as NMed45, it presents the same aspect ratio as Coa60, but $y^+ \approx 45$. The second grid is referred to as NMed30, it presents the same y^+ as Coa30, but $\mathit{AR} = 10$. The third grid has mesh parameters between these first two, $y^+ \approx 40$ and $\mathit{AR} = 7.5$, and is referred to as NMed40.

A grid with the same spacing as Med30 is tested with $y^+ \approx 40$ and $\mathit{AR} = 5$ and referred to as Med40.

Two additional grids with different characteristics are also tested: NFine35 having spacing 3mm, $y^+ \approx 35$ and $\mathit{AR} = 4.29$; and BMed30 having spacing 5mm, $y^+ \approx 30$ and $\mathit{AR} = 8.33$. In Figure 8 the grids location on the y^+, AR plane is shown. Notice that the grids tested in the second stage are highlighted in black. The dashed line represents the constraint imposed by (3).

Mesh characteristics and standard notation used for the new grids are summarized in Table 4.

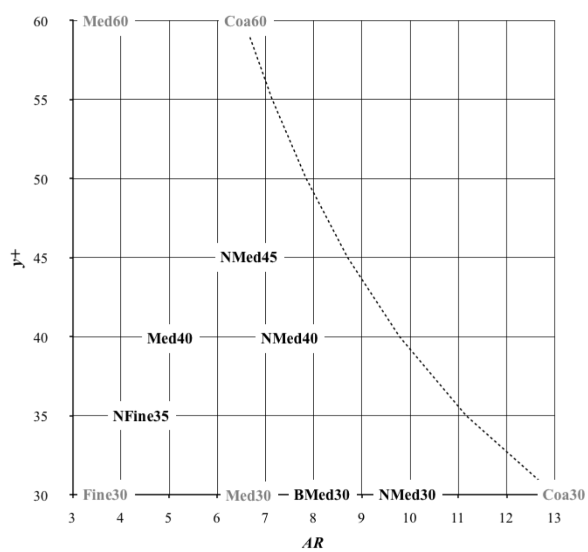

Figure 8. Grid positions on the y^+, AR plane.

1. *Results*

Among the new grids tested in this stage, the best performances are that of NFine35SA and Med40SA. They both follow with good approximation the experimental C_l versus ride height curve, correctly predict the maximum in downforce at $h = 0.134c$ and present a mean error below 2% for NFine35SA and below 4% for Med40SA. With both grids separation at the trailing edge is firstly observed at $h = 0.179c$.

NMed40SA also predicts a decent C_l versus ride height curve, but shows an higher average error, above 5%.

BMed30SA presents a smaller average error, below 5%, but at $h = 0.134c$ the predicted downforce coefficient shows a plateau instead of a maximum.

Less accurate are the performances of NMed30SA and NMed45SA. In fact, they both fail to predict the maximum in downforce at the correct ride height and with NMed45SA oscillations in the converged results are observed.

All NMed40SA, BMed30SA, NMed30SA and NMed45SA predict a first hint of separation at the trailing edge at $h = 0.224c$, in agreement with experiments. Also in this stage, with all the grids tested a large area of separation is observed at $h = 0.09c$.

In Figure 9 the downforce coefficient versus ride height curves for all the grids tested with *Spalart-Allmaras* are depicted and in Figure 10 the errors in the solutions for every ride height in the considered range are given in percentage of the experimental value.

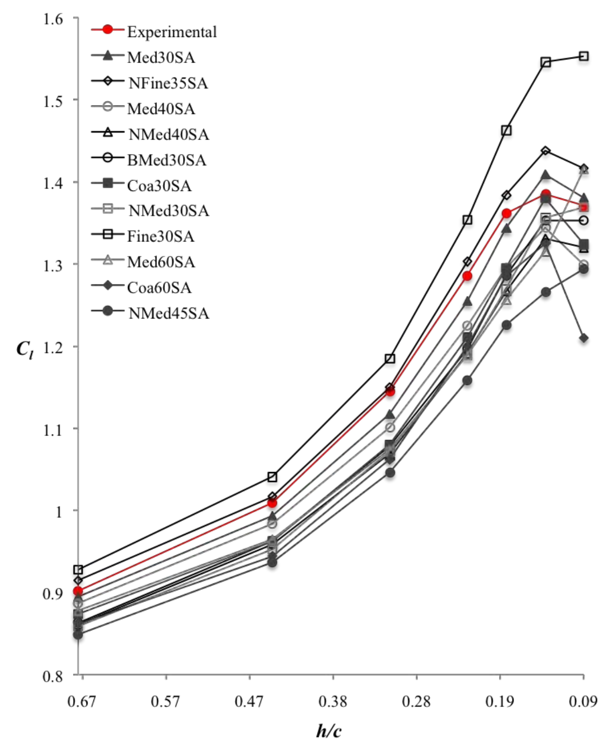

Figure 9. Downforce coefficient versus ride height for all grids tested with *Spalart-Allmaras* in ride height sensitivity study.

On the base of their performance, all the grids tested with *Spalart-Allmaras* in the ride height sensitivity study, are divided in 4 categories: *Red, Orange, Light Green* and *Green*, with *Red* representing the worst grids and *Green* the best ones.

The performance of the grids is judged on the basis of 4 parameters: absolute value of average and maximum error, correct prediction of the downforce maximum at $h = 0.134c$ and absence of oscillations in the solutions.

Grids that fulfill all the requirements and have an average error below 5% fall into the *Green* category; these are Med30, NFine35 and Med40. Grids that show oscillations in the solutions or did not capture the maximum in downforce at the correct ride height, and have an average error above 5% fall into the *Red* category; these are Fine30, Med60, Coa60, NMed45. The remaining ones are classified either in the *Orange* or the *Light Green* category. A schematic summary of the categorization can be found in Table 5.

Following this categorization the portion of the $y^+, \text{Æ}$ plane where a certain grid belongs to, is colored accordingly to that grid category. An interpolation rule is chosen to color the remainder of the plane (Figure 11).

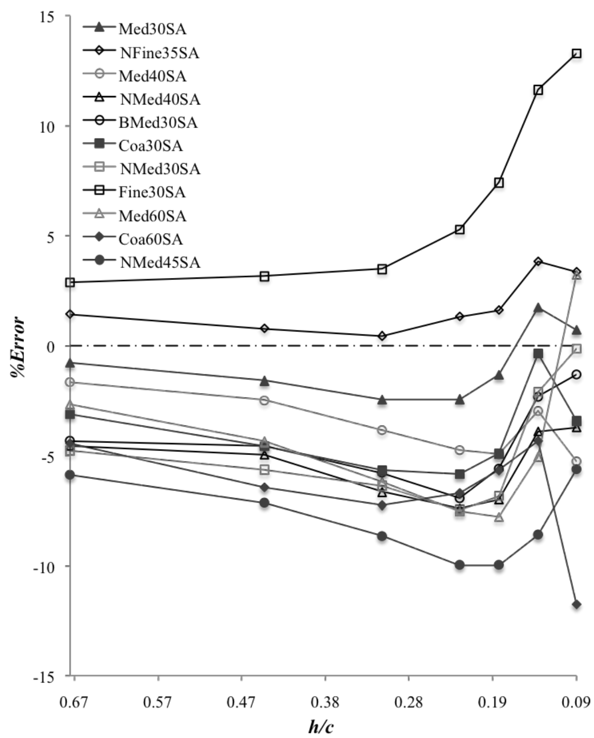

Figure 10. Errors given in percentage of the experimental downforce coefficient for the grids tested with *Spalart-Allmaras*.

2. *Discussion*

From the outcome of the ride height sensitivity study it can be concluded that a major role in affecting simulation results is not only played by mesh characteristics alone, but also by the combination of these. In particular, an optimal area of mesh parameter combinations can be identified on the $y^+, \text{Æ}$ plane. The boundaries of this area are given by $4 < \text{Æ} < 7$ and $30 \leq y^+ \leq 40$.

Moving to the left of this area means decreasing the Æ of the first cell and this adversely influences the results. Why this is so should be investigated further. One of the reasons can be that wall functions work better on a more stretched cell.

On the other hand increasing the Æ has a more gradual effect: moving to the right of the optimal area causes first an increase in the difference between predicted C_l and experimental results, followed by problems with delayed separation so that the maximum in downforce is postponed to lower ride heights, and finally convergence problems are observed due to the coarsening of the mesh.

The upper limit of y^+ determines the range in which the wall function correctly approximate the boundary layer. This depends in the first place on the turbulence model used. For instance, from the previous results it can be concluded that with *Realizable* $k - \epsilon$ the maximum y^+ for which good results can still be found, would be lower. On the other hand, it also depends on how the wall function is implemented in the solver.

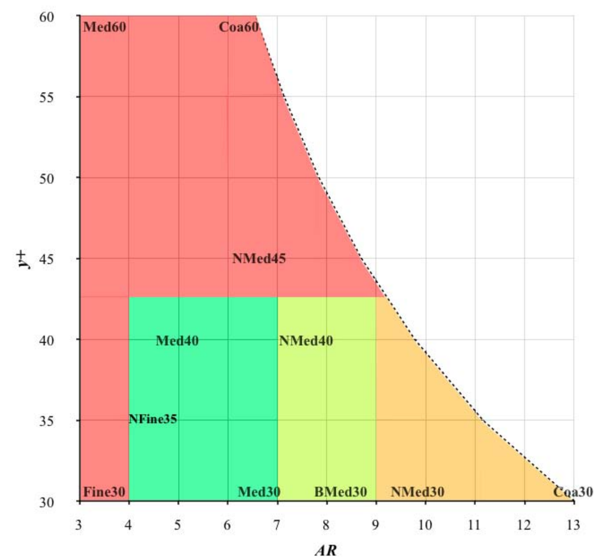

Figure 11. Grid positions and categorization on the y^+, Æ plane.

V. Conclusions and Recommendations

The aerodynamics of a 2D single element wing in ground effect has been numerically investigated. The effect of grid refinement, mesh parameters, turbulence models, boundary layer modeling and ride height was examined. Overall the obtained results are in agreement with previous experimental results and they are more accurate compared to computational studied found in literature.[5,15,17]

Better results were obtained when modeling the boundary layer with a wall function than solving the equations up to the wall. Nonetheless decent results were obtained with *Launder-Sharma* $k - \epsilon$. This model also demonstrated a very low grid sensitivity.

A dependence of the solution on combinations of mesh parameters has been investigated. In particular, it has been shown that an optimal range of $y^+/\AE R$ exists for which the physics of an inverted airfoil in ground effect can be correctly modeled by solving RANS equations.

The most accurate prediction of the downforce coefficient was obtained with *Spalart-Allmaras* with wall function. The model has shown robustness for a larger range of grid parameters and ride heights compared to the other turbulence models tested. In particular *Realizable* $k-\epsilon$ displayed higher sensitivity on y^+ values, whereas $k-\omega$ *SST* had problems at the smaller ride heights where the large area of separated flow and consequent drop in downforce was not observed.

On the basis of the results obtained in the present research, some recommendations for future work may be suggested:

- It should be verified whether the conclusions drawn for the airfoil can be extended to a more complex 3D model.
- The reason why the finest grid tested with wall function did not give the best results has to be investigated further.
- It is advised to run simulations with different solvers in order to better interpret the solutions of *Realizable* $k-\epsilon$ and $k-\omega$ *SST* and validate to what extend their performance was influenced by the way the models are implemented into OpenFOAM.
- The effect of simulating or specifying transition from laminar to turbulent flow should be analyzed.

References

[1]Davidson, P. A., *Turbulence; An Introduction for Scientists and Engineers*, Oxford University Press, 2004.

[2]Godin, P., Zingg, D. W., Nelson, T. E., *High-Lift Aerodynamic Computations with One- and Two-Equation Turbulence Models*, AIAA Journal, Vol. 35, No. 2, Feb 1997, pp. 237-243.

[3]Katz, J., *Aerodynamics of Race Cars*, Annual Review of Fluid Mechanics, Vol. 38, Jan 2006, pp. 27-63.

[4]Lopez, A. M. G., Carvalheira, P., *On the Application of Numerical Methods for the Calculation of External Aerodynamics of a Streamlined Car Body*, SAE Technical Paper 2003-01-1249, in Vehicle Aerodynamics 2003.

[5]Mahon, S., Zhang, X., *Computational Analysis of Pressure and Wake Characteristics of an Aerofoil in Ground Effect*, Journal of Fluid Engineering, Transaction of the ASME Vol. 127, March 2005, pp. 290-298.

[6]Mahon, S., Zhang, X., *Computational Analysis of an Inverted Double-Element Airfoil in Ground Effect*, Journal of Fluid Engineering, Transaction of the ASME Vol. 128, Nov. 2006, pp. 1172-1180.

[7]Makowsky, F. T., Kim, S. E., *Advances in External-Aero Simulation of Ground Vehicles Using the Steady RANS Equations*, SAE Technical Paper 2000-01-0484, in Vehicle Aerodynamics 2000.

[8]Menter, F. R., *Improved Two-equation $k-\omega$ Turbulence Models for Aerodynamic Flows*, NASA Technical Memorandum 103975, Oct. 1992.

[9]Mokhatar, W. A., *A Numerical Study of High-Lift Single Element Airfoils with Ground Effect for Racing Cars*, SAE Transactions, Vol. 114, No. 6, 2005, pp. 682-688.

[10]Ranzenbach, R., Barlow, J., *Two-dimensional Airfoil in Ground Effect; an Experimental and Computational Study*, SAE Technical Paper 94-2509, 1994.

[11]Ranzenbach, R., Barlow, J., *Cambered Airfoil in Ground Effect; Wind tunnel and Road Conditions*, 13th AIAA Applied Aerodynamics Conference, AIAA, Washington, DC, 1995, pp. 1208-1215

[12]Ranzenbach, R., Barlow, J., *Cambered Airfoil in Ground Effect; an Experimental and Computational Study*, SAE Technical Paper 96-0909, 1996.

[13]Shih, T. H., Liou, W. W., Shabbir, A., Yang, Z., Zhu, J., *A New $k-\epsilon$ Eddy Viscosity Model for High Reynolds Number Turbulent Flows-Model; Development and Validation*, NASA Technical Memorandum 106721, Aug. 1994.

[14]Spalart, P., Allmaras, S., *A One-Equation Turbulence Model for Aerodynamic Flows*, AIAA Paper 92-0439, 1992.

[15]Zerihan, J., Zhang, X., *Aerodynamics of a Single Element Wing in Ground Effect*, Journal of Aircraft, Vol. 37, No. 6, 2000, pp. 1058-1064.

[16]Zerihan, J., *An Investigation into the Aerodynamics of Wings in Ground Effect*, Ph.D. Dissertation, School of Engineering Sciences, University of Southampton, Southampton, UK, 2001.

[17]Zerihan, J., Zhang, X., *A Single Element Wing in Ground Effect; Comparison of Experiments and Computation*, 39th AIAA Aerospace Sciences Meeting and Exhibit, Reno, NV, Jan 2001.

[18]Zerihan, J., Zhang, X., Toet, W., *Ground Effect Aerodynamics of Race Cars*, Annual Review of Fluid Mechanics, Vol. 59, No. 1, 2006, pp. 33-49.

Table 1. Coordinate listing of the airfoil Tyrrell026S.

x/c *suction*	y/c *suction*	x/c *pressure*	y/c *pressure*
0.0000	0.0000	0.0000	0.0000
0.0010	-0.0076	0.0010	0.0079
0.0020	-0.0107	0.0020	0.0109
0.0049	-0.0168	0.0051	0.0173
0.0099	-0.0228	0.0101	0.0232
0.0149	-0.0266	0.0151	0.0270
0.0199	-0.0293	0.0201	0.0299
0.0249	-0.0319	0.0251	0.0312
0.0298	-0.0344	0.0301	0.0321
0.0348	-0.0368	0.0351	0.0329
0.0398	-0.0392	0.0401	0.0336
0.0448	-0.0414	0.0451	0.0344
0.0498	-0.0436	0.0501	0.0352
0.0548	-0.0458	0.0551	0.0359
0.0598	-0.0479	0.0601	0.0367
0.0698	-0.0518	0.0701	0.0379
0.0797	-0.0554	0.0801	0.0392
0.0897	-0.0588	0.0902	0.0404
0.0997	-0.0619	0.1002	0.0413
0.1197	-0.0672	0.1202	0.0432
0.1396	-0.0713	0.1402	0.0446
0.1596	-0.0744	0.1602	0.0457
0.1796	-0.0763	0.1802	0.0465
0.1996	-0.0771	0.2002	0.0473
0.2496	-0.0753	0.2501	0.0489
0.2996	-0.0721	0.3001	0.0504
0.3496	-0.0679	0.3501	0.0514
0.3996	-0.0631	0.4001	0.0519
0.4496	-0.0574	0.4501	0.0521
0.4996	-0.0508	0.5001	0.0517
0.5497	-0.0434	0.5501	0.0509
0.5997	-0.0351	0.6001	0.0496
0.6497	-0.0261	0.6500	0.0479
0.6997	-0.0163	0.7000	0.0456
0.7498	-0.0056	0.7500	0.0429
0.7998	0.0060	0.8000	0.0409
0.8498	0.0183	0.8500	0.0412
0.8999	0.0315	0.9000	0.0446
0.9199	0.0370	0.9200	0.0468
0.9399	0.0426	0.9400	0.0496
0.9599	0.0484	0.9600	0.0527
0.9799	0.0543	0.9800	0.0563
0.9900	0.0573	0.9900	0.0583
1.0000	0.0603	1.0000	0.0603

Table 2. Mesh characteristics of grids tested with wall function.

Grid Name	Fine30	Med30	Med60	Coa30	Coa60
y^+	30	30	60	30	60
Element Length	2	4	4	8	8
First Layer Height	0.6	0.6	1.2	0.6	1.2
Aspect Ratio First Cell	3.33	6.67	3.33	13.33	6.67

Table 3. Mesh characteristics of grids tested with near wall treatment.

Grid Name	Fine05	Fine1	VFine05	Fine1
y^+	0.5	1	0.5	1
Element Length	2	2	1	1
First Layer Height	0.01	0.02	0.01	0.02
Aspect Ratio First Cell	200	100	100	50

Table 4. Mesh characteristics of additional grids used in the second stage of the ride height sensitivity study.

Grid Name	NFine35	Med40	BMed30	NMed30	NMed40	NMed45
y^+	40	40	30	30	40	45
Element Length	3	4	5	6	6	6
First Layer Height	0.7	0.8	0.6	0.6	0.8	0.9
Aspect Ratio First Cell	4.29	5	8.33	10	7.5	6.67

Table 5. Categorization of the *Spalart-Allmaras* grids used in the second stage of the ride height sensitivity study.

Grid	*Mean Error*	*Max Error*	$C_{l_{max}}$ *at* $h = 0.134c$	*Oscillations*	*Category*
Med30	0.868	2.445	Yes	No	Green
NFine35	1.827	3.827	Yes	No	Green
Med40	3.694	5.252	Yes	No	Green
NMed40	5.446	7.387	Yes	No	Light Green
BMed30	4.396	6.921	No*	No	Light Green
Coa30	3.983	5.832	Yes	Yes	Orange
NMed30	4.761	7.465	No	No	Orange
Fine30	6.763	13.275	No	No	Red
Med60	4.342	7.783	No	Yes	Red
Coa60	6.649	11.743	Yes	Yes	Red
NMed45	7.972	9.985	No	Yes	Red

* The downforce coefficient shows a plateau.

Table 6. Results of grid and turbulence model sensitivity study.

	Free Stream		$h = 0.224c$		$h = 0.09c$	
Case Name	C_l	*Error %*	C_l	*Error %*	C_l	*Error %*
Experimental	0.766		1.286		1.371	
Spalart-Allmaras	0.885	15.535	1.475	14.697	1.539	12.254
$k - \omega$ *SST*	0.872	13.838	1.352	5.132	1.297	-5.398
Fine30RKE	0.825	7.702	1.285	-0.078	2.086	52.152
Fine30KWS	0.820	7.050	1.437	11.742	2.136	55.799
Fine30SA	0.805	5.091	1.354	5.288	1.553	13.275
Med30RKE	0.749	-2.219	1.258	-2.177	1.250	-8.826
Med30KWS	0.779	1.697	1.306	1.555	1.779	29.759
Med30SA	0.777	1.436	1.255	-2.411	1.381	0.729
Med60RKE	0.730	-4.700	1.050	-18.351	1.750	27.644
Med60KWS	0.789	3.003	1.306	1.555	1.737	26.696
Med60SA	0.767	0.131	1.189	-7.543	1.415	3.209
Coa30RKE	0.750	-2.089	1.140	-11.353	1.218	-11.160
Coa30KWS	0.766	0.000	1.145	-10.964	1.585	15.609
Coa30SA	0.762	-0.522	1.211	-5.832	1.324	-3.428
Coa60RKE	0.714	-6.789	1.008	-21.617	1.045	-23.778
Coa60KWS	0.770	-0.522	1.130	-12.131	1.425	3.939
Coa60SA	0.762	-0.522	1.200	-6.687	1.210	-11.743
Fine05LSKE	0.787	2.742	1.297	0.855	1.520	10.868
Fine05SA	0.835	9.008	1.449	12.675	1.900	38.585
Fine1LSKE	0.777	1.436	1.267	-1.477	1.525	11.233
Fine1SA	0.833	8.747	1.445	12.364	1.888	37.710
VFine05LSKE	0.784	2.350	1.303	1.322	1.525	11.233
VFine05SA	0.848	10.705	1.505	17.030	2.000	45.879
VFine1LSKE	0.775	1.175	1.264	-1.711	1.525	11.233
VFine1SA	0.845	10.313	1.495	16.252	1.975	44.055

Mean Results

Grid	C_l	*Error %*	C_l	*Error %*	C_l	*Error %*
Fine30	0.817	6.614	1.359	5.651	1.925	40.408
Med30	0.768	0.305	1.273	-1.011	1.470	7.221
Med60	0.762	-0.522	1.182	-8.113	1.634	19.183
Coa30	0.759	-0.870	1.165	-9.383	1.376	0.340
Coa60	0.749	-2.263	1.113	-13.478	1.227	-10.528
Fine05	0.811	5.875	1.373	6.765	1.710	24.726
Fine1	0.805	5.091	1.356	5.443	1.707	24.471
VFine05	0.816	6.527	1.404	9.176	1.763	28.556
VFine1	0.810	5.744	1.380	7.271	1.750	27.644
Turbulence Model	C_l	*Error %*	C_l	*Error %*	C_l	*Error %*
RKE	0.754	-1.619	1.148	-10.715	1.470	7.206
KWS	0.785	2.454	1.265	-1.649	1.732	26.360
SA - *wf*	0.775	1.123	1.242	-3.437	1.377	0.408
LSKE	0.781	1.926	1.283	-0.253	1.524	11.142
SA - *nwt*	0.840	9.693	1.474	14.580	1.941	41.557

Appendix

Drag Coefficient

In Figure 1 and Figure 2 the drag coefficient versus ride height curves, for all the combinations grid-turbulence model tested in the ride height sensitivity study, is depicted. The predicted downforce and drag coefficients are reported in Table 1.

Unlike the downforce, the drag has a monotone behavior: it increases with decreasing ride height and no maximum and subsequent drop is observed. This is so because, for higher ride heights, the friction drag increases together with the downforce. On the other hand, for smaller ride heights, separation occurs so, even though the friction drag drops, the additional pressure drag due to separation prevents the total drag to decrease.

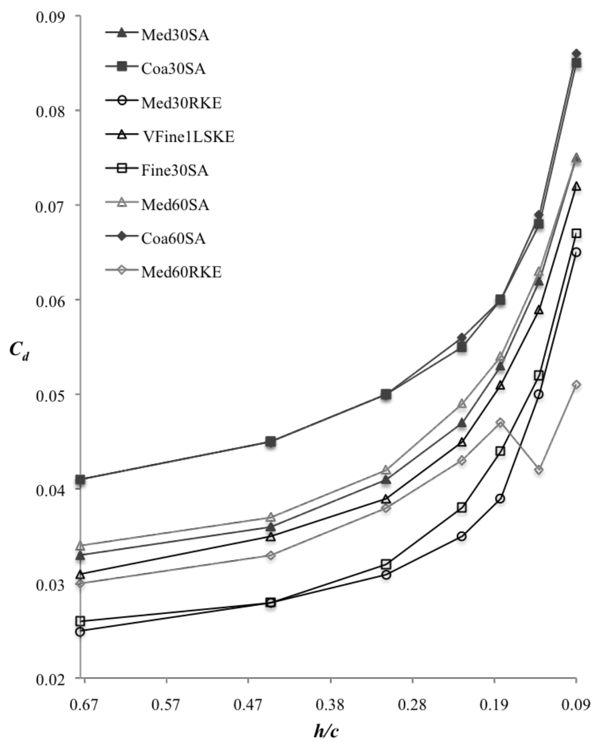

Figure 1. Drag coefficient versus ride height for the combinations grid-turbulence model tested in the first stage of the ride height sensitivity study.

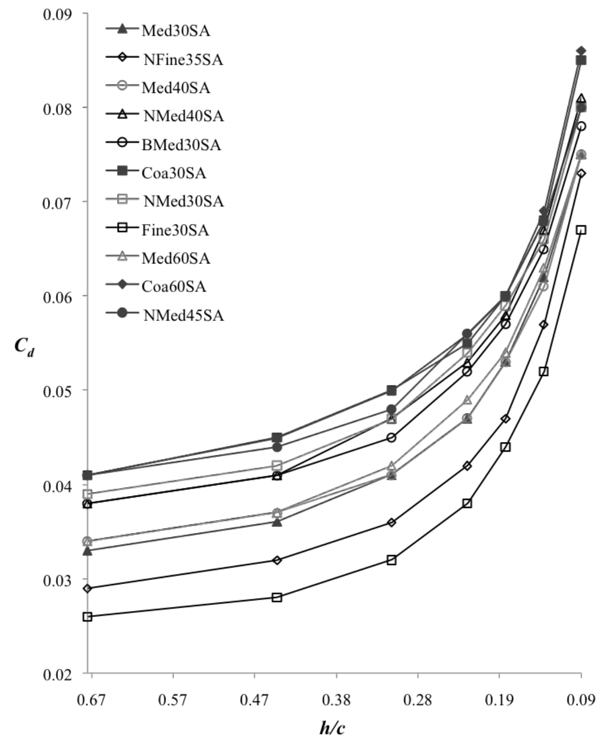

Figure 2. Drag coefficient versus ride height for the combinations grid-turbulence model tested in the second stage of the ride height sensitivity study.

No comparison with experimental results has been possible but, for all the combinations tested, the trend of the predicted curves is correct. The only exception is Med60RKE that, also in this case, gives the least accurate performance observed.

Pressure Coefficient

In Figure 3 the pressure coefficient predicted with Med30SA for all the tested ride heights is shown.

It is possible to see how the negative pressure peak is always found on the lower point of the suction surface, in correspondence with the throat of the Venturi channel that forms between the airfoil and the ground.

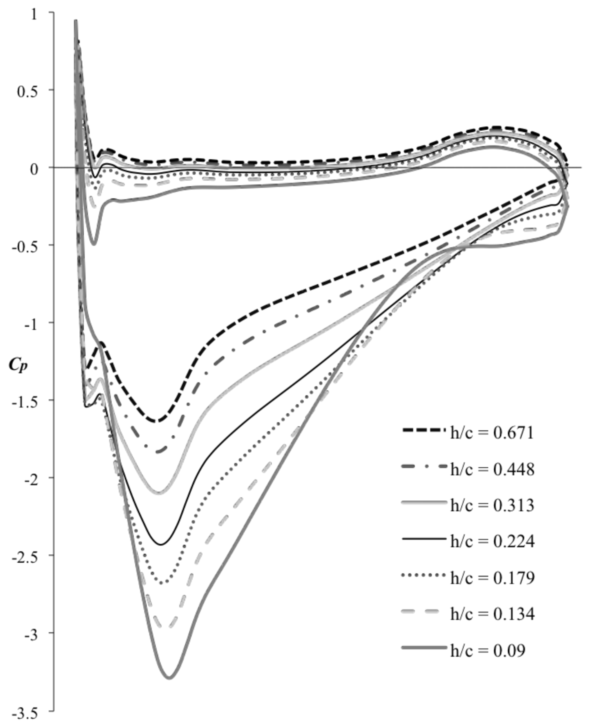

Figure 3. Pressure coefficient for Med30SA at all the ride heights considered in the ride height sensitivity study.

It is also interesting to notice how, at the smallest ride heights, the pressure coefficients on the suction surface shows a plateau at the trailing edge, a clear indication of the fact that no pressure recovery is achieved and separation is present.

Laminar Computations

Some laminar computations have been performed in order to assess the benefits of using a turbulence model and quantify the differences in terms of error with respect to experimental results. The grids Fine30 and Med30 have been tested at three significant ride heights: free stream, $h = 0.224c$ and $h = 0.09c$. The predicted downforce coefficient is compared with the one obtained using *Spalart-Allmaras*. Results are summarized in Table 2.

In Figure 4 the errors in percentage of the experimental downforce coefficients are given for the three ride heights.

As it is shown in the picture, in free stream the downforce coefficient predicted with laminar computations is similar to the turbulent one, for both grids.

At $h = 0.224c$ the largest difference in predicted downforce is found: for Fine30 the error rises from 5%, obtained with *Spalart-Allmaras*, to almost 29% with laminar computations. Analogously for Med30 the error rises from 2.4% to 29%.

At the smaller ride height while for Fine30 the error decreases to 1% with laminar computations, for Med30 it goes from almost zero to 13%.

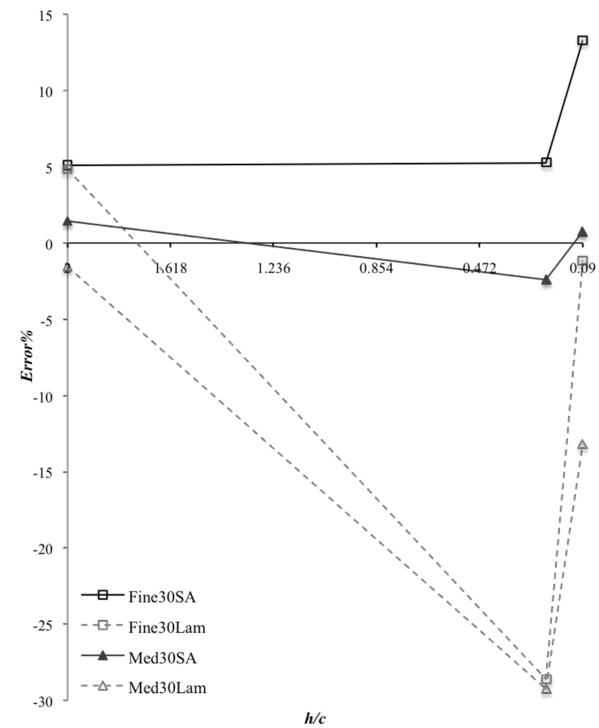

Figure 4. Comparison in terms of error with respect to experiments of the performances of laminar and turbulent computations.

From the results it can be inferred that the use of a turbulence model is of fundamental importance, especially at the medium ride heights, where the laminar computations predict values of the downforce coefficients much different from the experiments, compared to the turbulent ones.

Furthermore in free stream, where the laminar and turbulent computations give very similar results, separation at the trailing edge is observed in the laminar cases, even though it is not reported in the experiments. The turbulent computations correctly predict attached flow.

At the smaller ride height tested, the difference between turbulent and laminar computations decreases, probably because of a "laminarizing" effect of the wall.

Table 1. Downforce and drag coefficients for all the combinations grid-turbulence model tested in the ride height sensitivity study.

	$h = 0.671c$		$h = 0.448c$		$h = 0.313c$		$h = 0.224c$		$h = 0.179c$		$h = 0.134c$		$h = 0.09c$	
Case Name	C_l	C_d	C_l	C_d	C_l	C_d	C_l	C_d	C_l	C_d	C_l	C_d	C_l	C_d
Med30SA	0.895	0.033	0.993	0.036	1.117	0.041	1.255	0.047	1.344	0.053	1.409	0.062	1.381	0.075
Coa30SA	0.874	0.041	0.963	0.042	1.08	0.047	1.211	0.054	1.295	0.059	1.38	0.066	1.324	0.08
Med30RKE	0.889	0.025	0.986	0.028	1.061	0.031	1.258	0.035	1.364	0.039	1.32	0.05	1.25	0.065
VFine1LSKE	0.887	0.031	0.99	0.035	1.12	0.039	1.264	0.045	1.357	0.051	1.457	0.059	1.525	0.072
Fine30SA	0.928	0.026	1.041	0.028	1.185	0.032	1.354	0.038	1.463	0.044	1.546	0.052	1.553	0.067
Med60SA	0.878	0.034	0.965	0.037	1.074	0.042	1.189	0.049	1.256	0.054	1.315	0.063	1.415	0.075
Coa60SA	0.862	0.041	0.944	0.045	1.062	0.05	1.2	0.056	1.285	0.06	1.325	0.069	1.21	0.086
Med60RKE	0.833	0.03	0.907	0.033	0.982	0.038	1.05	0.043	1.087	0.047	1.589	0.042	1.75	0.051
NFine35SA	0.915	0.029	1.017	0.032	1.15	0.036	1.303	0.042	1.384	0.047	1.438	0.057	1.417	0.073
Med40SA	0.887	0.034	0.984	0.037	1.101	0.041	1.225	0.047	1.295	0.053	1.344	0.061	1.299	0.075
NMed40SA	0.861	0.038	0.959	0.041	1.069	0.047	1.191	0.053	1.267	0.058	1.331	0.067	1.32	0.081
BMed30SA	0.863	0.038	0.963	0.041	1.079	0.045	1.197	0.052	1.286	0.057	1.353	0.065	1.353	0.078
NMed30SA	0.859	0.039	0.952	0.042	1.072	0.047	1.19	0.054	1.269	0.059	1.356	0.066	1.369	0.08
NMed45SA	0.849	0.041	0.937	0.044	1.046	0.048	1.158	0.056	1.226	0.06	1.266	0.068	1.294	0.08

Table 2. Comparison between downforce coefficients obtained using a turbulence model and laminar simulations for the grids Fine30 and Med30.

	Fine30					Med30			
	Experimental	*Spalar-Allamras*	*Error %*	*Laminar*	*Error %*	*Spalar-Allamras*	*Error %*	*Laminar*	*Error %*
Free Stream	0.766	0.805	5.091	0.803	4.830	0.777	1.436	0.754	−1.566
$h = 0.224c$	1.286	1.354	5.288	1.000	−28.600	1.255	−2.411	0.910	−29.238
$h = 0.09c$	1.371	1.553	13.275	1.355	−1.167	1.381	0.729	1.190	−13.202

A CFD Investigation of a Bluff Body Equipped with a Diffuser in Ground Effect

Emanuela Genua

Delft University of Technology, Delft 2629HS, The Netherlands

Actiflow BV, Breda 4823AD, The Netherlands

A computational study of the flow around a bluff body equipped with a diffuser in ground effect is performed. The effect of geometric parameters, turbulence model, grid refinement, computational domain, ground simulation and use of the complete, rather than half model, is throughly investigated. Results are compared to previous work in literature. The main features of the flow are captured. Nonetheless, a certain discrepancy in terms of ride height at which physical phenomena take place is observed. The numerical solutions are not very sensitive to the choice of turbulence model, but *Spalart-Allmaras* shows a better agreement with the experiments in terms of flow separation.

Nomenclature

α	diffuser ramp angle
C_D	drag coefficient
C_L	downforce coefficient
C_P	pressure coefficient
d	half body width
h	ride height
l	body length
ν	kinematic air viscosity
p	static pressure
q_∞	free stream dynamic pressure
ρ	air density
Re	Reynolds number
u, v	velocity components
u_∞	free stream velocity
y^+	normalized distance from the wall

I. Introduction

The diffuser is a device of fundamental importance to the automotive industry. On the rear of a car it constitutes a region of upsweep that drives the air to a fixed pressure at the outlet, leading to a depression at the inlet, which generates downforce. In literature this phenomenon is referred to as *diffuser pumping*.[10,15,16] On a race car the diffuser can contribute up to one third of the total downforce.[18]

According to Ref. 18 the most extensive work on the subject of diffuser aerodynamics is due to Cooper et al.[4,5] Their experiments were conducted on a 3D bluff body equipped with a diffuser in ground effect. The ground was simulated using a moving belt system. Reducing the ground clearance they observed the phenomena of downforce enhancement, maximum downforce and downforce reduction. The reason given for the downforce reduction phenomenon was the merging of the body and ground boundary layers.

A more recent work was performed by Zhang et al.[13,15,16] In Ref. 16 force and pressure behaviour of a bluff body equipped with a 17° diffuser operating in ground effect were investigated by Senior and Zhang. With respect to the ride height, four distinct regions of downforce behavior were distinguished: downforce enhancement region, maximum downforce region, downforce reduction region and low downforce region.

In the force enhancement region, as the body is lowered to the ground, the flow beneath the model is accelerated and the pressure at the diffuser inlet decreases, which increases the downforce coefficient. As the ride is reduced the adverse pressure gradient over the diffuser ramp becomes larger and larger until separation takes place. Reducing the ride height even further this separation line moves forward. This range of ride heights is what Senior and Zhang referred to as maximum downforce region and is characterized by a plateau in downforce coefficient. The maximum is found between $h = 0.21d$ and $h = 0.217d$, where d is half body width. When the model is brought even closer to the ground, the downforce drops abruptly, presumably as consequence of asymmetric separation at the diffuser inlet.

Since the critical ride height at which downforce reduction occurred was observed to be independent of the Reynolds number, they inferred that the physical phenomenon causing the downforce reduction could not be the merging of the boundary layers as described by Cooper et al.[4,5]

According to Senior and Zhang the boundary layer merging phenomenon exists, but is more likely to be found in the low downforce region. Here the downforce remains low and it is not very sensitive to further ride height reduction. This could be attributed to reduced flow entering the diffuser due to the size of the boundary layers.

In Ref. 13 Ruhrmann and Zhang investigated the effect of the diffuser angle on the same bluff body used in Ref. 16. The angles tested were 5, 10, 15, 17 and 20 degrees. They identified two different flow regimes depending on whether the diffuser angle was small (5, 10) or large (15, 17, 20).

For high angles the diffuser shows the same characteristics as found by Senior and Zhang in Ref. 16. For small angles no sudden downforce reduction was found. It was observed that for small diffuser angles no separation occurs and at low ride height the boundary layers form a large portion of the flow, causing direct transition from the maximum downforce region to the low downforce region. They also reported that normalizing the ride height with the diffuser angle, the maximum downforce occurs at similar values of $\frac{h}{d \cdot \alpha}$, approximately 0.7.

Extensive computational work on diffuser aerodynamics is due to Cooper et al.[4] They performed RANS simulations using the $k-\omega$ turbulence model. Their results were good overall for a 9.17° diffuser. On the other hand they were not very successful when simulating a 13.5° diffuser. The drag was overpredicted and for small ride height the downforce behaviour was not in agreement with the experimental results; the plateau in downforce coefficient was not observed in the computational results.

In this paper a numerical investigation into the aerodynamics of a bluff body equipped with a diffuser in ground effect is reported. The goal of this research is to establish to what extend it is possible to correctly model the complex flow dynamics described so far with CFD. The effect of geometric parameters, turbulence model, grid refinement, computational domain, ground simulation and use of the complete, rather than half model, is assessed.

II. Computational Modeling

A. Geometry

The numerical investigation will be performed on the same diffuser equipped bluff body used for experimental studies in Ref. 13, 15, 16. The original model is 1.315 m in length, 0.324 m in height and 0.314 m in width. The diffuser ramp has a $\alpha = 17°$ angle with respect to the horizontal and the inlet is located at $x = 0.777$ m. The distance between the body and the ground will be referred to as ride height h. In Figure 1 the geometry and coordinate system is depicted.

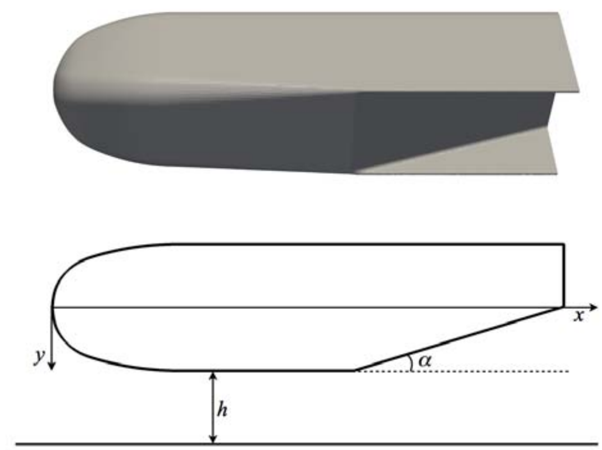

Figure 1. Bluff body geometry and coordinate system.

The model is equipped with side-plates. No information on the thickness of the side-plates is reported in literature. In the present study two different side-plates are tested: one was chosen wide enough to allow for good quality prism layers around it, the other one was as narrow as possible to draw. The former has a thickness of 10 mm and in the remainder of the paper will be referred to as thick side-plate, the latter has a thickness of 1 mm and will be referred to as thin side-plate. The two different side-plates are shown in Figure 2.

B. Flow Conditions

All the simulations are performed at a Reynolds number based on the body length of $1.8 \cdot 10^6$ corresponding to a free stream velocity of 20 m/s.

The free stream turbulence level has been set to 0.2%. These conditions correspond to the experimental conditions as given in Ref. 15, 16.

The integral length scale of the turbulence is set to 1 cm, typical for wind tunnel experiments.[1]

No transition from laminar to turbulent flow is simulated; the flow is assumed to be fully turbulent.

C. Governing Equations

The steady Reynolds-averaged Navier-Stokes equations are solved using OpenFOAM.

$$\frac{\partial \overline{u}_i}{\partial x_i} = 0 \tag{1}$$

$$\overline{u}_j \frac{\partial \overline{u}_i}{\partial x_j} = -\frac{1}{\rho}\frac{\partial \overline{p}}{\partial x_i} + \nu \frac{\partial^2 \overline{u}_i}{\partial x_j^2} - \frac{\partial \overline{u_i^{'} u_j^{'}}}{\partial x_j} \tag{2}$$

The turbulence is modeled with both *Spalart-Allmaras* and $k-\omega$ *SST*.

The convergence criterion is based on the aerodynamic forces on the body: when downforce and drag are observed to reach steady state values, simulations are stopped. The number of iterations required varies from 3000 to 6000.

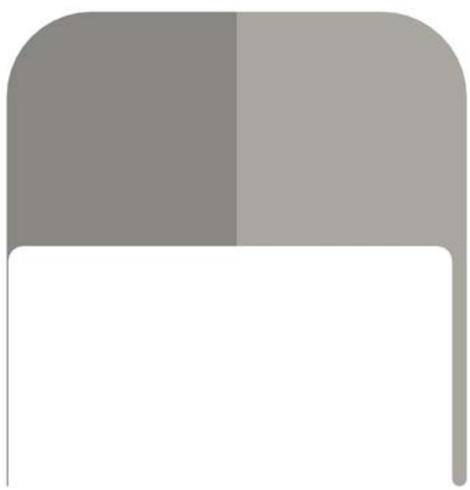

Figure 2. Comparison between thin (on the left) and thick side-plate (on the right).

D. Grid Structure

The computational grids are designed using ANSA. For different ride heights the general topology of the grid is fixed. Notice that for most of the computations, only half body is used.

Every mesh consists of three blocks: two prism layers are folded around the bluff body and along the ground, whereas the remainder of the computational domain is unstructured. In order to avoid severely non-orthogonal cells around the base of the model, no prism layers are used here.

Most of the cells on the body and ground surfaces are 9 mm in length. Smaller cells are used only when needed on the side-plates. The first layer of prismatic cells on body and ground is 1.4 mm high, corresponding to a $y^+ \approx 40$ and an aspect ratio of 6.43 defined as the length of the cell over the height. In total 6 layers are extruded, with a grow factor of 1.2. A detail of the mesh on the body surface is shown in Figure 3.

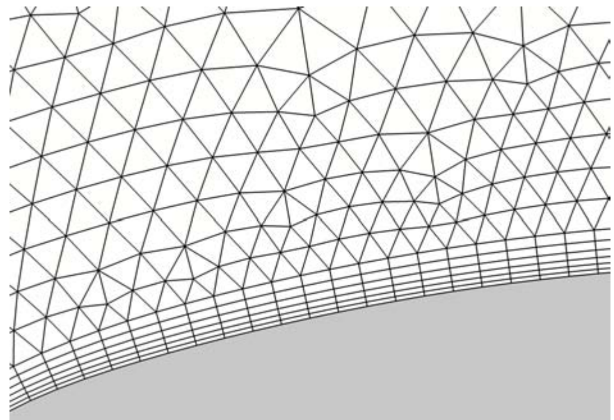

Figure 3. A particular of the prism mesh folded around the bluff body.

The upstream and downstream boundaries of the computational domain are placed respectively at 4 and 10 body lengths from the nose. The distance of the upper boundary from the ground and the width of the computational domain is 4 body lengths.

Depending on the ride height and on the thickness of the side-plates the total number of cells varies from 8 to 10 million.

E. Boundary Conditions

The bluff body and ground plane are modeled as solid walls at which a no-slip boundary condition is imposed. Furthermore, in order to correctly simulate the ground effect, on the ground plane a tangential velocity equal to the free stream speed is prescribed.

At the upstream boundary a uniform velocity inlet and a zero pressure gradient condition are prescribed, whereas at the downstream boundary a zero velocity gradient and a uniform pressure outlet are imposed.

The top boundary of the computational domain and the symmetry plane are modeled as slip walls.

III. Ride Height Sensitivity Study

A ride height sensitivity study is performed. The ride height range investigated goes from $h = 0.764d$ to $h = 0.064d$.

Half body with both thick and thin side-plates is used for all the computations.

Abbreviations are used to identify the turbulence model in the case name: SA and KWS indicate *Spalart-Allmaras* and $k - \omega$ *SST*, respectively. Furthermore, if the model is equipped with the thin side-plate the extension 'sp' is used in the case name.

All the results in this paper are compared to experimental results reported in Ref. 16.

Downforce and drag coefficients for all the ride heights and for all the tested cases are given in Table 1 and 2.

In Figure 4 and 5, the predicted downforce and drag versus ride height curves for all the tested cases are depicted.

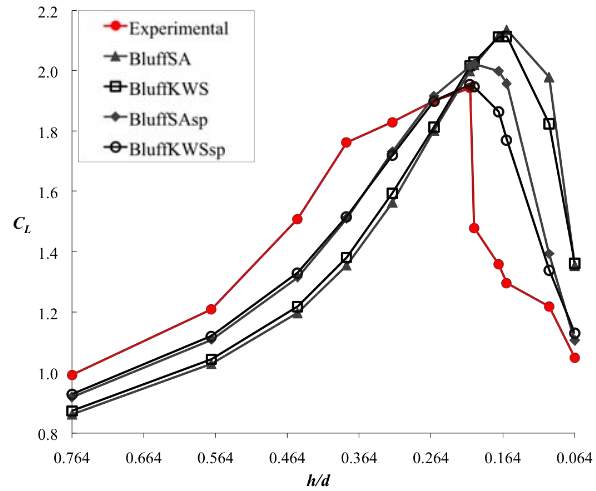

Figure 4. Downforce coefficient versus ride height for both turbulence models and side-plates tested.

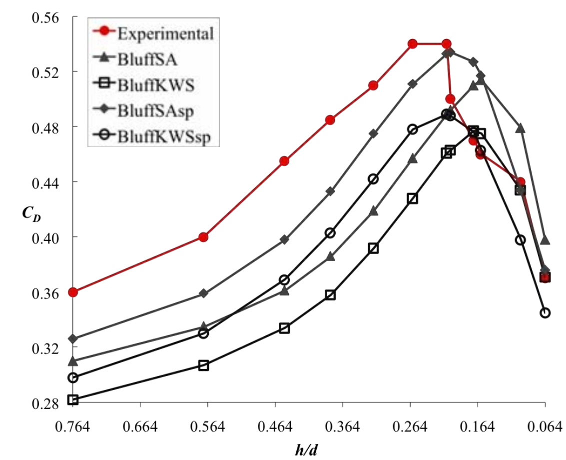

Figure 5. Drag coefficient versus ride height for both turbulence models and side-plates tested.

A. Results

1. *Thick Side-Plate*

Both turbulence models predict very similar downforce coefficients.

In the force enhancement region the C_L is always underpredicted of about 18% compared to experimental results, but the trend of the C_L versus ride height curve appears to be right.

The maximum in downforce is postponed to $h = 0.159d$. Here the largest difference in downforce coefficient between computations and experiments is found: with both turbulence models the predicted C_L is more than twice as big as the experimental value.

No plateau between $h = 0.382d$ and $h = 0.21d$ is observed in the computational results, the C_L continues to increase with approximately the same gradient until the maximum is reached.

With *Spalart-Allmaras* a region of separated flow on the diffuser ramp is observed for the first time at $h = 0.17d$. The separation increases with decreasing ride height until asymmetric separation at the diffuser inlet occurs at $h = 0.064d$. At this ride height a sudden drop in downforce is observed, in agreement with experiments.

$k - \omega$ *SST* predicts a very small region of separated flow at $h = 0.159d$. At $h = 0.1d$ a small portion of the flow is observed to separate both on the diffuser ramp and on the side plate. As for *Spalart-Allmaras* separation at the inlet of the diffuser and consequent sharp drop in downforce is predicted at $h = 0.064d$.

The predicted drag coefficient is more in agreement with the experimental results. The performance of *Spalart-Allmaras* is slightly better in terms of mean error (about 12%), but the maximum C_D is postponed to $h = 0.159d$. With $k - \omega$ *SST* the average error is about 14% and the maximum drag is found at $h = 0.17d$.

2. *Thin Side-Plate*

Also with the thin side-plate the two turbulence models give very similar downforce coefficients.

In the force enhancement region results are more in agreement with the experiments compared to the ones obtained with the thick side plate: the C_L is underpredicted of about 10%.

A region of downforce plateau is detectable, even though it is postponed to $0.26 \leq h/d \leq 0.17$. With $k - \omega$ *SST* the maximum in C_L and C_D is correctly predicted at $h = 0.21d$ while with *Spalart-Allmaras* it is postponed to a slightly smaller ride height, $h = 0.204d$.

As for the thick side-plate *Spalart-Allmaras* predicts first separation on the diffuser ramp at $h = 0.17d$ while this is not observed with $k - \omega$ *SST* at any ride height. With both models separation at the diffuser inlet starts at $h = 0.1d$. At this ride height a sudden drop in downforce is observed.

Again the computed drag coefficient is closer to the experiments. *Spalart-Allmaras* and $k - \omega$ *SST* give an average error with respect to experiments of about 7% and 10% respectively.

B. Discussion

From the results it can be inferred that the thickness of the side-plate has a major impact on the predicted downforce and drag coefficients. In particular this geometric parameter determines the amount of side flow entering the underbody. The more high pressure flow enters the underbody, the more the pumping effect of the diffuser is neutralized. This in turn entails a lower predicted value for C_L.

In Figure 6 a comparison in terms of pressure coefficient underneath the diffuser ramp with thick and thin side-plate is depicted. The figure shows the pressure coefficient contour plot obtained with *Spalart-Allmaras* at $h = 0.45d$ on the plane $x = 0.91$. From the picture it can be inferred that with the thin side-plate less flow enters the underbody preserving a low pressure between the side-plate and the diffuser ramp.

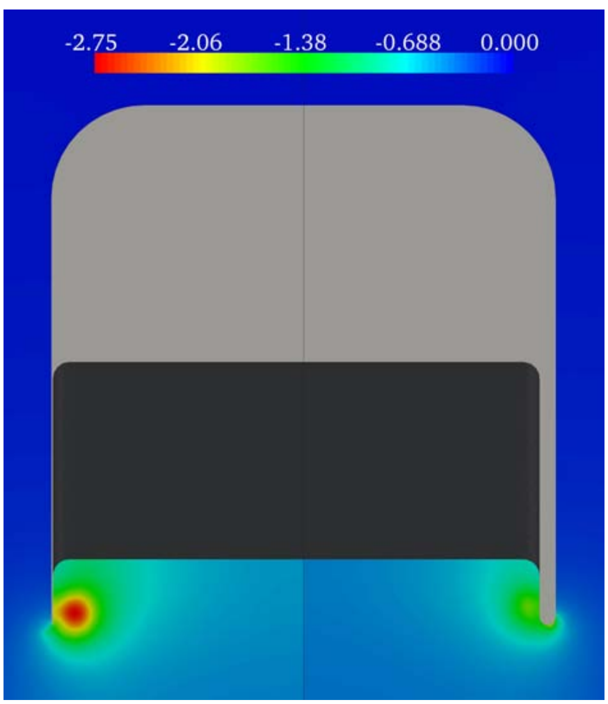

Figure 6. Comparison between the pressure coefficient contour plot on the plane $x = 0.91$ obtained with *Spalart-Allmaras* at $h = 0.45d$ for the thin side-plate model on the left and for the thick side-plate model on the right.

Shifting from the thick side-plate to the thin one, the C_L and C_D versus ride height curves move upwards, towards a better approximation of the experimental results.

The choice of turbulence model does not seem to have a significant effect on the computational force coefficients. Nonetheless, *Spalart-Allmaras* showed to have better predictive capabilities on flow dynamic phenomena such as separation patterns.

The surface pressure coefficient underneath the diffuser ramp along the centerline for the model with thin side-plate obtained with *Spalart-Allmaras* and $k - \omega$ *SST* is depicted in Figure 7 and Figure 8, respectively. From the figures one can see that the negative pressure peak is always correctly predicted at the diffuser inlet $x = 0.777$ m with both turbulence model. Furthermore, reducing the ride height, the negative pressure peak increases until separation occurs and this trend is reversed, according to the experiments. It can also be noticed how the separation, represented in the figures as a plateau in pressure coefficient, moves forward with further reduction of the ride height.

From Figures 9, 10 and 11 one sees that *Spalart-Allmaras* predicts a surface flow separation pattern on the diffuser ramp very similar to the one observed in the experiments, even though it is postponed to smaller ride heights. Notice that the computations were performed on half body, then mirrored for the picture.

At smaller ride heights, in correspondence with the sharp drop in downforce, all the tested cases predicted separation at the diffuser inlet. In Figures 12 and 13 a comparison between experiments and computations is given.

In general, it appears that the main features of the flow are captured: the force enhancement until a maximum is reached and the subsequent sharp drop due to asymmetric separation at the diffuser inlet. However a delay in terms of ride height at which these phenomena occur is present. This delay can be due to different side plates geometry or to a disparity in predicted boundary layer thickness between computations and experiments which would make ground proximity less important, shifting all the related physical phenomena to smaller ride heights. Unfortunately neither of these hypotheses can be further investigated because no data were reported in literature about the side-plate geometry and the measured boundary layer thickness.

IV. Sensitivity Study

In an effort to investigate different reasons other than the aforementioned ones that could explain the gap between computational and experimental results, a sensitivity study on several parameters is performed:

- The effect of mesh refinement is assessed.
- In the hypothesis that the proximity of the model to the wind tunnel walls could affect the experimental results, a computational domain having the same dimensions as the test section employed in Ref. 16 is used.
- Since asymmetric phenomena are reported to take place, the effect of simulating the flow over the entire bluff body is investigated.
- In order to evaluate whether a deficiency in the wind tunnel ground simulation system could have affected experimental results, a comparison is made between computational and experimental results on fixed ground.

The sensitivity study is performed at three significant ride heights:

- The height $h = 0.45d$ is chosen as representative of the downforce enhancement region, where the downforce generated by the bluff body increases with reducing ride height.
- The height $h = 0.21d$ is chosen as representative of the maximum downforce region. According to experiments at this ride height a large area of separated flow on the diffuser ramp is present.
- The height $h = 0.159d$ is chosen as representative of the downforce reduction region, where the downforce generated by the bluff body suddenly decreases because of asymmetric separation at the inlet of the diffuser.

A. Results

1. Mesh Refinement

For the generation of the finer meshes the topology of the grid is maintained.

Most of the cells on the body and ground surfaces are 6 mm in length. Smaller cells are used only when needed on the side-plates. The first layer of prismatic cells on body and ground is 1.2 mm high, corresponding to a $y^+ \approx 35$ and an aspect ratio of 5. In total 9 layers are extruded, with a grow factor of 1.1.

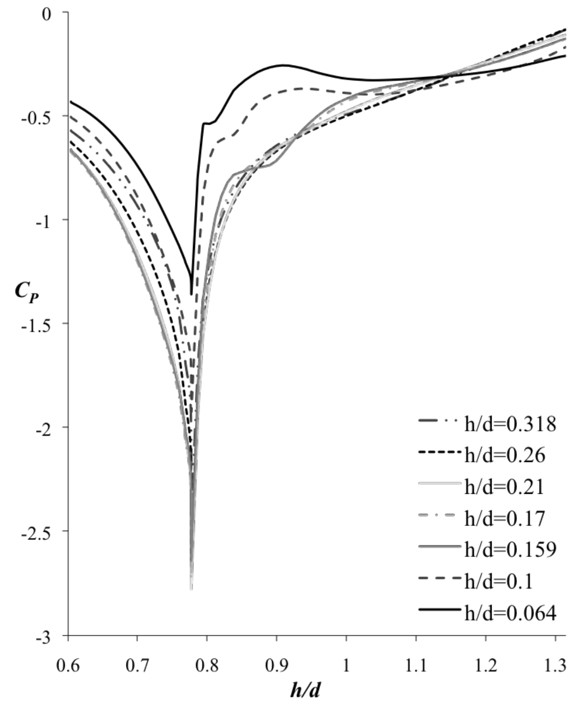

Figure 7. Pressure coefficient on the diffuser ramp along the centerline obtained with *Spalart-Allmaras* on the thin side-plate model for different ride heights.

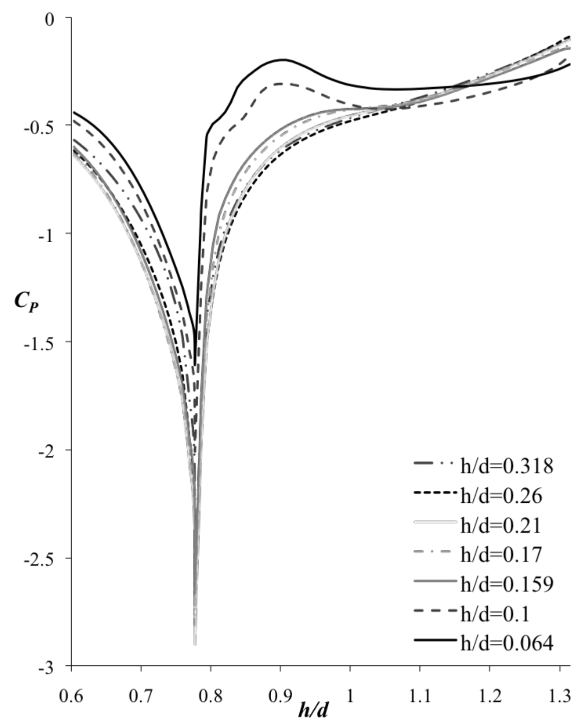

Figure 8. Pressure coefficient on the diffuser ramp along the centerline obtained with $k-\omega$ *SST* on the thin side-plate model for different ride heights.

Notice that the mesh refinement cases are indicated with a '6' in the name, before the abbreviation of the turbulence model.

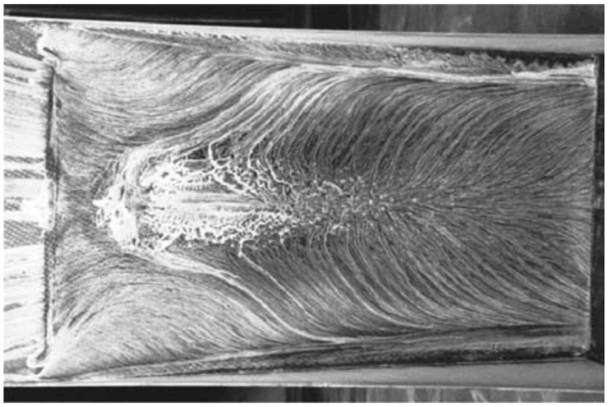

Figure 9. Surface flow pattern at $h = 0.217d$. Taken from Ref. 16.

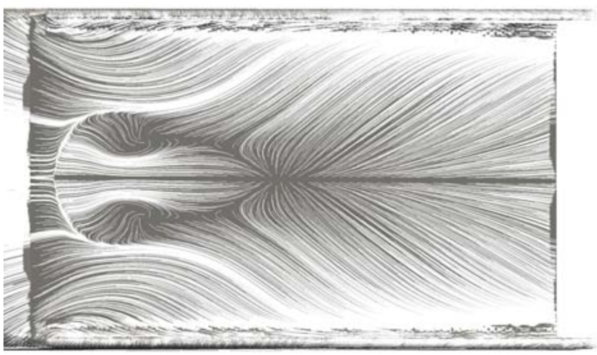

Figure 10. Surface flow pattern obtained with *Spalart-Allmaras* on the thick side-plate model at $h = 0.1d$.

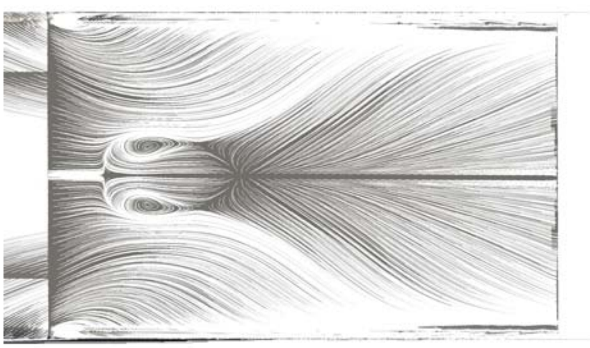

Figure 11. Surface flow pattern obtained with *Spalart-Allmaras* on the thin side-plate model at $h = 0.159d$.

Depending on the ride height and on the thickness of the side-plates the total number of cells varies from 20.6 to 21.5 million.

With this mesh the number of iterations required to reach convergence varies from 3000 to 8000.

In Table 3 all the results are summarized. A comparison is made between the force coefficient predicted by all the cases tested in the ride height sensitivity study and the ones obtained with the refined mesh for the considered ride heights.

It appears that mesh refinement has no significant impact on the predicted C_L and C_D. On average there is a 1% difference in the predicted values of the downforce and drag coefficients compared to the ride height sensitivity study, with a maximum of 4% for Bluff6KWS at $h = 0.159d$.

2. Computational Domain

The test section of the wind tunnel used in Ref. 16 is 2.1 m wide, 1.5 m high and 4.4 m long.

Since only half model is used in the numerical simulations, the computational domain is taken 1.05 m wide and 1.5 m high. Furthermore the upstream and downstream boundaries are placed at 1.3 m and 3.1 m from the body nose, respectively. The side and upper boundaries of the computational domain are still modeled as slip walls.

Notice that the simulations with the described computational domain are indicated with the initials 'SB' in the case name, before the abbreviation of the turbulence model.

The same mesh parameters as described in the ride height sensitivity study are used. Depending on the ride height and on the thickness of the side-plates the total number of cells varies from 2.4 to 2.8 million. The number of iterations required to reach convergence varies from 3000 to 6000.

In Table 4 all the results are summarized. A comparison is made between the force coefficient predicted by all the cases tested in the ride height sensitivity study and the ones obtained with the smaller computational domain for the considered ride heights.

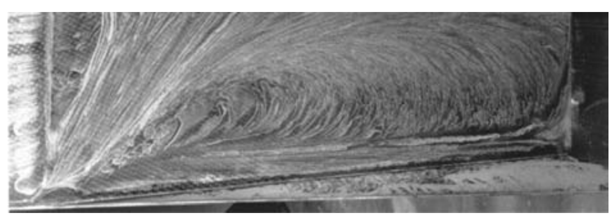

Figure 12. Surface flow pattern at $h = 0.191d$. Taken from Ref. 16.

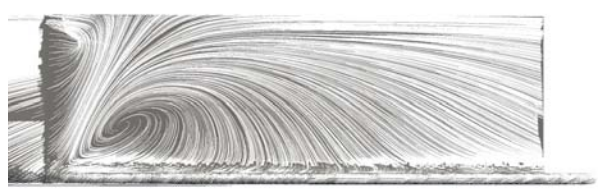

Figure 13. Surface flow pattern obtained with *Spalart-Allmaras* on the thick side-plate model at $h = 0.064d$.

From the results it can be seen that the size of the computational domain has little influence on the predicted C_L and C_D. In particular, the average difference in force coefficients with respect to the ride height sensitivity study is about 4%, with a maximum of 6.6% for BluffSBSA at $h = 0.45d$.

Notice that this small difference is always positive, it does not seem to drive the computational results towards a better agreement with the experiments.

3. Complete Body

For these simulations the entire model is used. The mesh characteristics are the same as described in the ride height sensitivity study and the computational domain is twice as wide. Depending on the ride height and on the thickness of the side-plates the total number of cells varies from 16.2 to 19.7 million. The number of iterations required to reach convergence varies from 3000 to 10000. Notice that the simulations ran with the complete model are indicated with '2X' in the case name, before the abbreviation of the turbulence model.

At this stage, also a ride height representative of the low downforce region is considered, $h = 0.064d$. The surface flow pattern obtained at this ride height with Bluff2XSA and Bluff2XKWS are shown in Figure 15 and Figure 16 in comparison with experimental results shown in Figure 14. Notice that, while *Spalart-Allmaras* predicts asymmetric flow according to the experiments, with $k - \omega$ *SST* separation occurs at both sides of the diffuser inlet.

All the results are summarized in Table 5. A comparison between the force coefficient predicted by all the cases tested in the ride height sensitivity study and the ones obtained with the complete body for the considered ride heights is shown in Figure 17 and 18.

From the results it can be inferred that numerically simulating the flow over the entire model, rather than over half of it, does not significantly affect the predicted values of downforce and drag coefficients. On average there is a 1% difference in C_L and C_D with respect to the ride height sensitivity study.

The only exception to this is represented by Bluff2XKWSsp at the ride height $h = 0.159d$: the downforce and drag coefficient are about 30% and 20% smaller than the ones obtained with half model. While for the downforce coefficient this means a decrease in the error with respect to experimental results from 36% to 5%, for the drag coefficient is the other way around: the error rises from 0.7% to 18%.

In order to better investigate this anomaly, Bluff2XKWSsp is tested on two additional ride heights: $h = 0.204d$ and $h = 0.1d$. The results are summarized in Table 6. Notice that for these ride heights the results are in line with the trend observed so far, with an average difference of 2% with respect to the results obtained with half model.

Furthermore, after the sharp drop in downforce at $h = 0.159d$, more in agreement with the experiments compared to the previous computations, the C_L is observed to grow again, towards the computational results found with the half body and against the general trend of downforce coefficient versus ride height.

Figure 14. Surface flow pattern at $h = 0.191d$. Taken from Ref. 16.

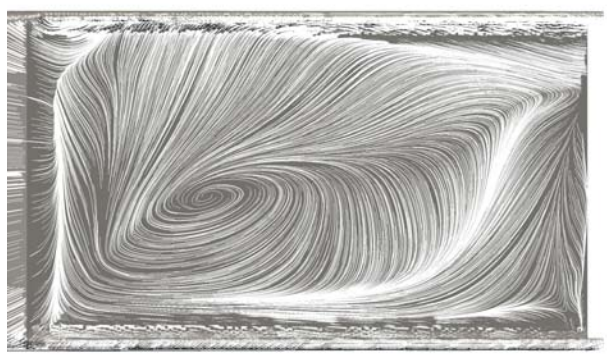

Figure 15. Surface flow pattern obtained with *Spalart-Allmaras* on the thick side-plate model at $h = 0.064d$.

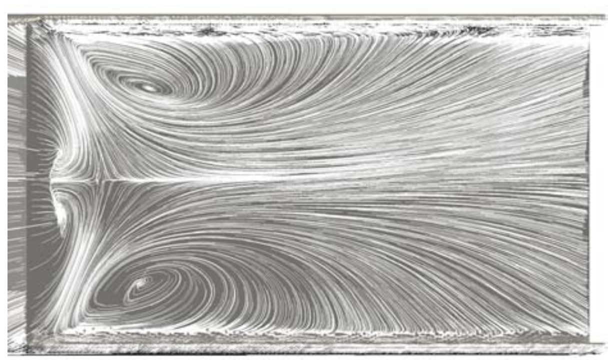

Figure 16. Surface flow pattern obtained with $k - \omega$ *SST* on the thick side-plate model at $h = 0.064d$.

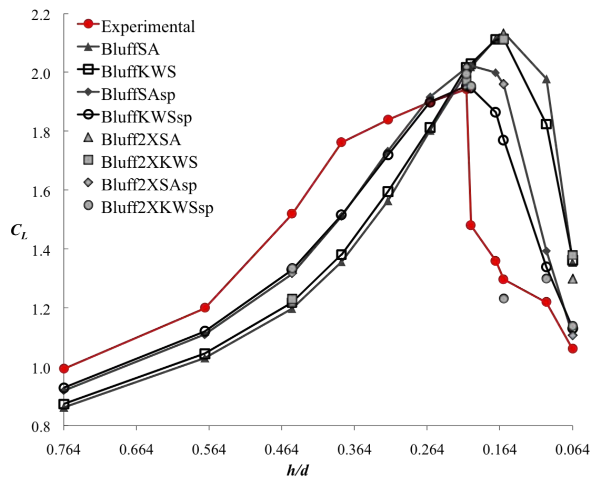

Figure 17. Comparison between the downforce coefficient obtained in the ride height sensitivity study and the one obtained using the complete body.

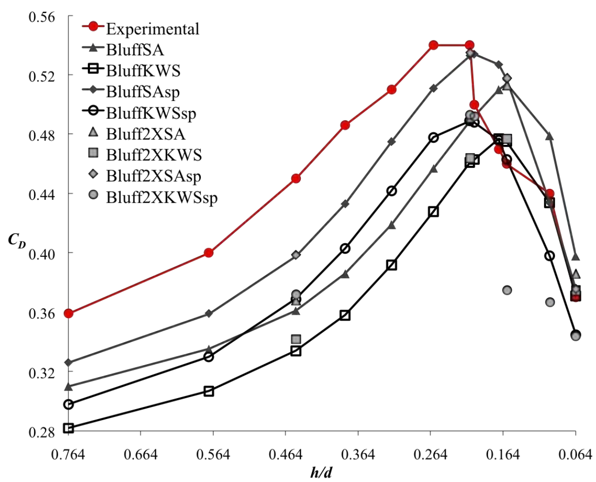

Figure 18. Comparison between the drag coefficient obtained in the ride height sensitivity study and the one obtained using the complete body.

Considering this phenomenon and the worsening of the drag coefficient prediction, the performance of Bluff2XKWSsp at $h = 0.159d$ seems to be an isolated case which does not significantly affect the interpretation of the results obtained so far.

4. *Fixed Ground*

In Ref. 16 the downforce coefficient versus ride height obtained when using a fixed ground is given for $Re = 1.8 \cdot 10^6$.

In Table 7 the computational results are compared to experiments for the considered ride heights. Notice that the simulations ran with fixed ground are indicated with the initials 'FG' in the case name, before the abbreviation of the turbulence model.

The same mesh characteristics and computational domain as described in the ride height sensitivity study are used. For these simulations the number of iterations required to reach convergence varies from 5000 to 6000.

Notice that also with fixed ground simulations the error with respect to experimental results in the force enhancement region is still quite large, about 20%, then it gets smaller around the downforce maximum, about 6%, and grows again in the downforce reduction region, about 20%.

B. Discussion

The computational results obtained in the ride height sensitivity study show to be very robust to changes.

For all the considered parameters and ride heights, the new force coefficient are very similar to the ones obtained in the ride height sensitivity study. The only exception to that is represented by Bluff2XKWSsp at $h = 0159d$, the performance of which has been investigated thoroughly.

Therefore, in the effort to understand the reason for the discrepancies between experiments and computations, mesh refinement, dimensions of the computational domain, the use of the entire rather than half model and ground simulations have to be ruled out.

Also a time dependent calculation has been ran on the complete model with thick side-plate using *Spalart-Allmaras*, but the result did not show better agreement with the experiment.

V. Conclusions and Recommendations

The aerodynamics of a bluff body equipped with a diffuser in ground effect has been numerically investigated. The effect of side-plates geometry, turbulence model, grid refinement, computational domain, ground simulation and use of the complete rather than half model has been examined.

The predicted downforce and drag coefficients versus ride height curves show a similar trend compared to experiments. Nonetheless, in the numerical simulations a certain delay in terms of ride height at which physical phenomena take place is observed.

The choice of turbulence model appeared to have little influence on the computational force coefficient. However *Spalart-Allmaras* showed a better agreement with the experiments in terms of flow separation.

Among the other parameters considered, the geometry of the side-plate seemed to have a major influence on the computational results. The numerical solutions did not show significant sensitivity to any of the other parameters object of the investigation.

The most accurate performance was observed when thin side-plates and the *Spalart-Allmaras* turbulence model were used. Even so a disparity between experimental and computational results was detectable; however, given the robustness shown by the computational results a new experimental investigation is advised.

On the basis of the results obtained in the present research, some recommendations for future work may be suggested:

- The reason of the disparities between the results reported in the present work and in literature has to be investigated further with the aid of new experimental studies.
- The effect of solving the equations up to the wall rather than using a turbulence model should be assessed.
- It is advised to run simulations with a different solver in order to validate to what extent the performance of the turbulence models was influenced by the way they are implemented into OpenFOAM.
- The effect of simulating or specifying transition from laminar to turbulent flow should be analyzed.

References

[1]Davidson, P. A., *Turbulence; An Introduction for Scientists and Engineers*, Oxford University Press, 2004.

[2]Aronson, D., Brahim, S. B., Perzon, S., *On the Underbody Flow of a Simplified Estate*, SAE Technical Paper 2000-01-0485, in Vehicle Aerodynamics 2000.

[3]Cogotti, A., *A Parametric Study on the Ground Effect of a Simplified Car Model*, SAE Technical Paper 980031, in Vehicle Aerodynamics 1998.

[4]Cooper, K. R., Bertenyi, T., Dutil, G., Syms, J., Sovran, G., *The Aerodynamic Performance of Automotive Underbody Diffusers*, SAE Technical Paper 980030, in Vehicle Aerodynamics 1998.

[5]Cooper, K. R., Sovran, G., Syms, J., *Selecting Automotive Diffusers to Maximize Underbody Downforce*, SAE Technical Paper 2000-01-0354, in Vehicle Aerodynamics 2000.

[6]Godin, P., Zingg, D. W., Nelson, T. E., *High-Lift Aerodynamic Computations with One- and Two-Equation Turbulence Models*, AIAA Journal, Vol. 35, No. 2, Feb 1997, pp. 237-243.

[7]Jones, M. A., Smith, F. T., *Fluid Motion for Car Undertrays in Ground Effect*, Journal of Engineering Mathematics, Vol. 45, 2003, pp. 309-334, Kluwer Academic Publishers.

[8]Katz, J., *Aerodynamics of Race Cars*, Annual Review of Fluid Mechanics, Vol. 38, Jan 2006, pp. 27-63.

[9]Lopez, A. M. G., Carvalheira, P., *On the Application of Numerical Methods for the Calculation of External Aerodynamics of a Streamlined Car Body*, SAE Technical Paper 2003-01-1249, in Vehicle Aerodynamics 2003.

[10]Mahon, S., Zhang, X., Gage, C., *The evolution of Edge Vortices Underneath a Diffuser Equipped Bluff Body*, 12th International Symposium on Applications of Laser Techniques to Fluid Mechanics, Lisbon, Portugal, Jul 2004.

[11]Makowsky, F. T., Kim, S. E., *Advances in External-Aero Simulation of Ground Vehicles Using the Steady RANS Equations*, SAE Technical Paper 2000-01-0484, in Vehicle Aerodynamics 2000.

[12]Menter, F. R., *Improved Two-equation $k-\omega$ Turbulence Models for Aerodynamic Flows*, NASA Technical Memorandum 103975, Oct. 1992.

[13]Ruhrmann, A., Zhang, X., *Influence of Diffuser Angle on a Bluff Body in Ground Effect*, Journal of Fluids Engineering, Transactions of the ASME, Vol. 125, March 2003, pp. 332-338.

[14]Sebben, S., *Numerical Flow Simulations of a Detailed Car Underbody*, SAE Technical Paper 2001-02-0703, in Vehicle Aerodynamics Design and Technology 2003.

[15]Senior, A. E., Zhang, X., *An Experimental Study of a Diffuser in Ground Effect*, 38th AIAA Aerospace and Sciences Meeting and Exhibit, Reno, NV, Jan 2000.

[16]Senior, A. E., Zhang, X., *The Force and Pressure of a Diffuser Equipped Body in Ground Effect*, Journal of Fluids Engineering, Transactions of the ASME, Vol. 123, March 2001, pp. 105-111.

[17]Spalart, P., Allmaras, S., *A One-Equation Turbulence Model for Aerodynamic Flows*, AIAA Paper 92-0439, 1992.

[18]Zerihan, J., Zhang, X., Toet, W., *Ground Effect Aerodynamics of Race Cars*, Annual Review of Fluid Mechanics, Vol. 59, No. 1, 2006, pp. 33-49.

Table 1. **Downforce coefficients for all the cases tested in the ride height sensitivity study and comparison with experiments.**

	Experimental	BluffSA		BluffKWS		BluffSAsp		BluffKWSsp	
h/d	C_L	C_L	*Error %*	C_L	*Error %*	C_L	*Error %*	C_L	*Error %*
0.764	0.993	0.862	−13.192	0.874	−11.984	0.919	−7.452	0.929	−6.445
0.570	1.210	1.030	−14.876	1.045	−13.636	1.109	−8.347	1.121	−7.355
0.450	1.510	1.198	−20.662	1.219	−19.272	1.316	−12.848	1.331	−11.854
0.382	1.763	1.356	−23.086	1.382	−21.611	1.511	−14.294	1.517	−13.953
0.318	1.830	1.564	−14.536	1.595	−12.842	1.733	−5.301	1.720	−6.011
0.260	1.900	1.803	−5.105	1.813	−4.579	1.917	0.895	1.900	0.000
0.210	1.943	2.000	2.934	2.017	3.809	2.016	3.757	1.954	0.566
0.204	1.480	2.019	36.419	2.030	37.162	2.023	36.689	1.947	31.554
0.170	1.360	2.115	55.515	2.113	55.368	1.999	46.985	1.865	37.132
0.159	1.297	2.136	64.688	2.114	62.992	1.958	50.964	1.771	36.546
0.100	1.220	1.979	62.213	1.825	49.590	1.394	14.262	1.340	9.836
0.064	1.050	1.355	29.048	1.363	29.810	1.106	5.333	1.131	7.714

Table 2. **Drag coefficients for all the cases tested in the ride height sensitivity study and comparison with experiments.**

	Experimental	BluffSA		BluffKWS		BluffSAsp		BluffKWSsp	
h/d	C_D	C_D	*Error %*	C_D	*Error %*	C_D	*Error %*	C_D	*Error %*
0.764	0.360	0.310	−13.889	0.282	−21.667	0.326	−9.444	0.298	−17.222
0.570	0.400	0.335	−16.250	0.307	−23.250	0.359	−10.250	0.330	−17.500
0.450	0.455	0.361	−20.659	0.334	−26.593	0.398	−12.527	0.369	−18.901
0.382	0.485	0.386	−20.412	0.358	−26.186	0.433	−10.722	0.403	−16.907
0.318	0.510	0.419	−17.843	0.392	−23.137	0.475	−6.863	0.442	−13.333
0.260	0.540	0.457	−15.370	0.428	−20.741	0.511	−5.370	0.478	−11.481
0.210	0.540	0.489	−9.444	0.461	−14.630	0.533	−1.296	0.489	−9.444
0.204	0.500	0.492	−1.600	0.463	−7.400	0.534	6.800	0.488	−2.400
0.170	0.470	0.510	8.511	0.477	1.489	0.527	12.128	0.476	1.277
0.159	0.460	0.514	11.739	0.475	3.261	0.517	12.391	0.463	0.652
0.100	0.440	0.479	8.864	0.434	−1.364	0.434	−1.364	0.398	−9.545
0.064	0.370	0.398	7.568	0.371	0.270	0.376	1.622	0.345	−6.757

Table 3. Comparison between downforce and drag coefficients obtained with the mesh used for the ride height sensitivity study and the refined mesh.

	$h = 0.450d$		$h = 0.210d$		$h = 0.159d$	
	C_L	C_D	C_L	C_D	C_L	C_D
BluffSA	1.198	0.361	2.000	0.489	2.136	0.514
Bluff6SA	1.216	0.366	2.003	0.495	2.115	0.515
Difference%	1.503	1.385	0.150	1.227	−0.983	0.195
BluffKWS	1.219	0.334	2.017	0.461	2.114	0.475
Bluff6KWS	1.232	0.341	1.987	0.466	2.028	0.474
Difference%	1.066	2.096	−1.487	1.085	−4.068	−0.211
BluffSAsp	1.316	0.398	2.016	0.533	1.958	0.517
Bluff6SAsp	1.310	0.392	2.018	0.529	1.984	0.518
Difference%	−0.456	−1.508	0.099	−0.750	1.328	0.193
BluffKWSsp	1.331	0.369	1.954	0.489	1.771	0.463
Bluff6KWSsp	1.320	0.366	1.953	0.488	1.808	0.468
Difference%	−0.826	−0.813	−0.051	−0.204	2.089	1.080

Table 4. Comparison between downforce and drag coefficients obtained with the computational domain used for the ride height sensitivity study and the smaller one

	$h = 0.450d$		$h = 0.210d$		$h = 0.159d$	
	C_L	C_D	C_L	C_D	C_L	C_D
BluffSA	1.198	0.361	2.000	0.489	2.136	0.514
BluffSBSA	1.252	0.385	2.038	0.517	2.141	0.539
Difference%	4.508	6.648	1.900	5.726	0.234	4.864
BluffKWS	1.219	0.334	2.017	0.461	2.114	0.475
BluffSBKWS	1.271	0.355	2.054	0.487	2.082	0.496
Difference%	4.266	6.287	1.834	5.640	−1.514	4.421
BluffSAsp	1.316	0.398	2.016	0.533	1.958	0.517
BluffSBSAsp	1.367	0.417	2.104	0.564	2.046	0.549
Difference%	3.875	4.774	4.365	5.816	4.494	6.190
BluffKWSsp	1.331	0.369	1.954	0.489	1.771	0.463
BluffSBKWSsp	1.381	0.385	2.036	0.518	1.858	0.492
Difference%	3.757	4.336	4.197	5.930	4.912	6.263

Table 5. Comparison between downforce and drag coefficients obtained with half and entire body.

	$h = 0.450d$		$h = 0.210d$		$h = 0.159d$		$h = 0.064d$	
	C_L	C_D	C_L	C_D	C_L	C_D	C_L	C_D
BluffSA	1.198	0.361	2.000	0.489	2.136	0.514	1.355	0.398
Bluff2XSA	1.221	0.368	1.959	0.491	2.133	0.513	1.300	0.386
Difference%	1.920	1.939	−2.050	0.409	−0.140	−0.195	−4.059	−3.015
BluffKWS	1.219	0.334	2.017	0.461	2.114	0.475	1.363	0.371
Bluff2XKWS	1.231	0.342	1.974	0.464	2.114	0.477	1.380	0.375
Difference%	0.984	2.395	−2.132	0.651	0.000	0.421	1.247	1.078
BluffSAsp	1.316	0.398	2.016	0.533	1.958	0.517	1.106	0.376
Bluff2XSAsp	1.319	0.399	2.019	0.535	1.961	0.518	1.108	0.376
Difference%	0.288	0.251	0.149	0.375	0.153	0.193	0.181	0.000
BluffKWSsp	1.331	0.369	1.954	0.489	1.771	0.463	1.131	0.345
Bluff2XKWSsp	1.336	0.372	1.995	0.493	1.232	0.375	1.140	0.344
Difference%	0.376	0.813	2.098	0.818	−30.435	−19.006	0.796	−0.290

Table 6. Comparison between downforce and drag coefficients obtained with half and entire body for Bluff2XKWSsp.

	$h = 0.204d$		$h = 0.159d$		$h = 0.1d$		$h = 0.064d$	
	C_L	C_D	C_L	C_D	C_L	C_D	C_L	C_D
BluffKWSsp	1.947	0.488	1.771	0.463	1.340	0.398	1.131	0.345
Bluff2XKWSsp	1.955	0.492	1.232	0.375	1.300	0.367	1.140	0.344
Difference%	0.410	0.820	−30.435	−19.006	−2.985	−5.528	0.796	−0.290

Table 7. Downforce and drag coefficients for fixed ground simulations and comparison with experiments.

	$h = 0.450d$		$h = 0.210d$		$h = 0.159d$	
	C_L	Error%	C_L	*Error*%	C_L	*Error*%
Experimental	1.360		1.780		1.360	
BluffFGSA	1.023	−24.809	1.712	−3.820	1.746	28.382
BluffFGKWS	1.036	−23.824	1.700	−4.494	1.709	25.662
BluffFGSAsp	1.118	−17.794	1.665	−6.461	1.559	14.632
BluffFGKWSsp	1.128	−17.059	1.618	−9.101	1.472	8.235

Conclusions and Recommendations

A CFD investigation into ground effect aerodynamics has been performed. In the first stage of the research the focus was on the aerodynamics of a 2D inverted single element wing. The effect of grid refinement, mesh parameters, turbulence models, boundary layer modeling and ride height was examined. Overall the obtained results are in agreement with previous experimental results and they are more accurate compared to computational studied found in literature.

Better results were obtained when modeling the boundary layer with a wall function than solving the equations up to the wall. Nonetheless decent results were obtained with *Launder-Sharma* $k-\epsilon$. This model also demonstrated a very low grid sensitivity.

A dependence of the solution on combinations of mesh parameters has been investigated. In particular, it has been shown that an optimal range of $y^+/Æ$ exists for which the physics of an inverted airfoil in ground effect can be correctly modeled by solving RANS equations.

The most accurate prediction of the downforce coefficient was obtained with *Spalart-Allmaras* with wall function. The model has shown robustness for a larger range of grid parameters and ride heights compared to the other turbulence models tested. In particular *Realizable* $k-\epsilon$ displayed higher sensitivity on y^+ values, whereas $k-\omega$ *SST* had problems at the smaller ride heights where the large area of separated flow and consequent drop in downforce was not observed.

With the aim of stepwise increasing the model complexity, in the second stage of the research the goal was to establish if and to what extent the results obtained on the 2D wing, namely the choice of grid parameters and turbulence model, could be extended to a simple 3D model. Within these objectives, the aerodynamics of a bluff body equipped with a diffuser has been numerically investigated. The effect of side-plates geometry, turbulence model, grid refinement, computational domain, ground simulation and use of the complete rather than half model has been examined.

The predicted downforce and drag coefficients versus ride height curves show a similar trend compared to experiments. Nonetheless the numerical results where not as much in agreement with the experiments as found for the airfoil: in the numerical simulations a certain delay in terms of ride height at which physical phenomena take place is observed.

The choice of turbulence model appeared to have little influence on the computational force coefficient. However, as for the profile, *Spalart-Allmaras* showed a better agreement with the experiments in terms of flow separation.

Among the other parameters considered, the geometry of the side-plate seemed to have a major influence on the computational results. The numerical solutions did not show significant sensitivity to any of the other parameters object of the investigation.

The most accurate performance was observed when thin side-plates and the *Spalart-Allmaras* turbulence model were used.

Performing unsteady simulations, both for the airfoil and the bluff body, did not show an improvement in the obtained results.

On the basis of this findings, some recommendations for a possible follow up thesis work may be suggested:

- The reason why the finest grid tested on the airfoil with wall function did not give the best results has to be investigated further.
- The effect of simulating or specifying transition from laminar to turbulent flow should be analyzed.
- It is advised to perform a solver sensitivity study in order to better interpret the results obtained with *Realizable* $k - \epsilon$ and $k - \omega$ *SST* and validate to what extend their performance was influenced by the way the models are implemented into OpenFOAM.
- Given the robustness shown by the computational results for the bluff body a new experimental investigation is suggested. With respect to the new experimental investigation, the discrepancies between wind tunnel and CFD results should be identified and quantified. Then the model complexity should be increased and validate whether the conclusions drawn for the simpler model could be extended to a real car model.